Multi-scale fracture network characterisation on carbonate platforms

Roberto Loza Espejel*, Tiago M. Alves and Tom G. Blenkinsop

3D Seismic Lab, School of Earth and Ocean Sciences, Cardiff University, Main Building – Park Place, CF10 3AT, Cardiff, United Kingdom

*Corresponding author:

Mobile phone: +44 7479 746160.

E-mail address: lozaespejelr@cardiff.ac.uk and lozaespejelr@gmail.com

Keywords: fracture networks; topology; geometry; outcrop analogue; carbonate platforms; fractured reservoirs

Abstract

Characterisation of fracture networks at different scales is challenging and important to many fields of geoscience, especially when access to multiple resolution datasets is limited. Here, we develop an integrated analysis of fracture networks on carbonate platforms using three scales of observation: small (outcrop), intermediate (airborne LiDAR) and large (3D seismic). Statistical analyses and ternary diagrams of geometrical and topological data from Cariatiz (South East Spain) and Pernambuco (East Brazil) are used to understand the relationships and distribution of fracture networks between multi-scale datasets. A variety of fracture types at each scale of observation reveal how complex fracture networks are on carbonate platforms. Our results demonstrate that fracture network properties behave differently depending on the fracture size, and that transitional scale gaps between datasets constrain fracture characterisation. Airborne LiDAR maps show that intermediate-sized fractures appear to have a better controlled orientation and a lower connectivity than smaller fractures from the same area in Cariatiz. Fracture branch length distributions fit a negative

exponential or log-normal distribution for massive non-stratabound units. This work is important as it demonstrates that the use of outcrop data is a good approach to understand fracture complexity of carbonate platforms. Understanding sub-seismic fracture networks is therefore critical in quantifying fluid flow and permeability in carbonate reservoirs.

1 Introduction

Fracture networks control many physical properties in rocks, and their characterisation is important in many disciplines of geosciences and engineering, including oil and gas exploration (Nelson, 2001; Sarkheil et al., 2013), geothermal reservoir characterisation (Chen et al., 2018; TerHeege et al., 2018; Vidal and Genter, 2018; Doornenbal et al., 2019), carbon capture and storage projects (March et al., 2018), hydrogeology and environmental geology studies (Abotalib et al., 2019; Medici et al., 2019), as well as mining and tunnelling (Friedman, 1975; Van As and Jeffrey, 2002; Zarei et al., 2012). Fracture networks have a significant effect on porosity, permeability and fluid flow of naturally fractured units. Well-connected open fractures can increase the natural permeability of rocks to provide active conduits for fluid flow (Laubach, 2003; Maerten et al., 2006; Strijker et al., 2012; Gutmanis et al., 2018). Conversely, closed or cemented fractures can act as barriers compartmentalising reservoirs, which is important for field delineation (Bourbiaux, 2010). Examples of fractured carbonate reservoirs can be found worldwide including the Cantarell complex in Campeche (Gulf of Mexico), the Haft Kel field in North Iraq (Middle East), and the Ekofisk complex in the North Sea (Dominguez et al., 1992; Key et al., 1999; Hermansen et al., 2000; Alavian and Whitson, 2005; Mandujano et al., 2005; Bourbiaux, 2010; Santiago et al., 2014; Galvis, 2018).

A key aspect in reservoir characterisation is the need to analyse the interaction between individual fractures and fracture sets, which can be estimated by studying topological attributes such as branch and node types (Strijker et al., 2012; Sanderson and Nixon, 2015). Both geometrical and topological attributes affect the connectivity and permeability of a rock volume. Moreover, natural fractures typically occur over several orders of magnitude; they range from microscopic fissures to kilometre structures such as fracture swarms or corridors (Bush, 2010). It is therefore crucial to understand the scale dependency of these distribution parameters to characterise sub-surface fluid flow patterns (Berkowitz, 2002; Tao and Alves, 2019).

Fractures can be described by quantifiable geometrical attributes such as their orientation, length, height, spacing, morphology, or some other form of classification involving fracture type and mineral fill (Odling et al., 1999). In this paper, we use the term *fracture* for any type of discontinuity (joints, faults, etc.) formed in different settings, such as during large-scale tectonic events, local uplift and erosion, slope instability or excess fluid pressure (Peacock et al., 2000, 2016; Berkowitz, 2002; Kim and Sanderson, 2005). The intention is to characterise an entire fracture network, including different fracture types of various sizes that interact between each other within a given rock unit, as all of them may contribute to the connectivity of the fracture network. Specific terms such as fault, joint, fracture swarm, etc. are only used where the fracture type and geological connotation are important to the analysis.

1.1 Challenges and limitations

One of the main challenges when characterising fracture networks is to obtain reliable data to analyse fracture networks at different scales. At present, it is still difficult to fully characterise fractures from a single dataset or by utilising data in which fractures of certain sizes cannot be observed due to limited data resolution. Integration of datasets and the knowledge of the capabilities for each type of data are key. Ideally, a carbonate platform with access to an exhaustive dataset, allowing mapping at different scales in both surface (e.g. outcrop mapping, drone imagery, airborne LiDAR) and sub-surface (e.g. cores, borehole, seismic), would provide a comprehensive setting to fully characterise not just fracture networks, but also additional structural and sedimentological properties. However, availability of such a perfect scenario is rare, and the necessity to work with limited datasets is a daily issue for geoscientists.

Three-dimensional (3D) reflection seismic data is usually the main source of subsurface structural information in industry. Seismic surveys are generally acquired at a line spacing of 25 to 50 m and, depending on the resolution of the seismic volume, faults with throws smaller than 10 to 30 m cannot be resolved (Needham et al., 1996; Lohr, 2004; Maerten et al., 2006). Faults and fractures of sizes below seismic resolution, referred to as sub-seismic, can only be determined using borehole data (e.g. wireline logs, cores, well log images), leading to underestimations of fracture volumes (Maerten et al., 2006). Fracture downscaling or upscaling using discrete stochastic methods is a common practice to populate fractures with a scale that cannot be observed directly from the studied dataset, for example between seismic and borehole data (Cacas et al., 2001; Chilès, 2005). Similarly, fractal analyses have been undertaken to characterise fracture properties (Needham et al., 1996; Nicol et al., 1996; Bonnet et al., 2001). However, their scale invariance is still subject to controversy (Cowie et al., 1996; Needham et al., 1996; Nicol et al., 1996; Gillespie et al., 2001; Guerriero et al., 2010), and extrapolations with limited reliable statistics can lead to important uncertainties (Maerten et al., 2006).

Outcrop analogues play an important role in the evaluation of small- and intermediate-scale fracture parameters that cannot be quantified from seismic and borehole data (e.g. Eberli et al., 2005; Gutmanis et al., 2018, Fig.4). Field analogues can guide the development of conceptual reservoir models and provide spatial and statistical data to understand inter-well fracture property populations, as techniques are available to cover all scales of observation (Nelson, 2001; Strijker et al., 2012; Gutmanis and Ardèvol i Oró, 2015; Sanderson, 2016). In such analyses, it is important to carefully choose valid field analogues to calibrate them with reservoir data (Cacas et al., 2001; Laubach et al., 2009; Kleipool et al., 2017). If there is sufficient exposure of fracture data, and sampling is undertaken carefully using appropriate methodologies (e.g. circular scanlines), field analogues can provide valuable information to characterise 3D fracture networks in multi-scale scenarios (Bertotti et al., 2007; Strijker et al., 2012).

This study is not an exception of the challenges associated to data limitations; in fact, we aim to emphasise the issues associated when characterising multi-scale fracture networks. For this reason, an integrated methodology is explained in detail, utilising three scales of observation from two carbonate platforms with similar settings. This approach allowed us to characterise fractures at sub-seismic (centimetre to metre) and seismic (kilometre) scales.

The Cariatiz carbonate platform in the Sorbas Basin, SE Spain, which has a unique 3D exposure, was used to analyse the geometry and topology of fracture networks at two sub-seismic scales from outcrop mapping (small scale) and airborne LiDAR (Light Detection and Ranging) maps (intermediate scale) (Fig. 1). Correlating the two datasets, covering the same carbonate platform, allowed us to predict trends of fracture properties at different scales. In addition, three-dimensional (3D) seismic studies from the Pernambuco carbonate platform in East Brazil were used to analyse km-long fracture networks (Fig. 2). Comparison between the two study areas (Cariatiz and Pernambuco) have limitations as they are not in the same region. However, they are of great importance to improve the understanding of multi-scale fracture networks (Fig. 3). Outcrop data provides the opportunity to understand sub-seismic fractures that can be used as conceptual models when only working with seismic data. In contrast, seismic data is useful to understand km-long fractures that are often poorly exposed, and can also be used as conceptual models for example, when working with borehole data or surface data.

This study is a novel approach to study multi-scale fracture networks. However, there is indeed the possibility and a call to continue future work to test and apply our observations and conclusions in similar carbonate platforms which might have a more robust dataset covering fracture sizes of several orders of magnitude in the same region. This paper addresses the following research questions:

a) How can we improve interpretation techniques combining fracture datasets with different resolutions to predict sub-seismic fractures?
b) What is the importance of integrating geometrical and topological attributes in the study of fracture networks?
c) What is the complexity of natural fracture networks at sub-seismic scales?
d) Do fractures of distinct sizes observed at different scales present different attributes?

In summary, this work analyses the relationship between fracture sizes to test if there is a correlation between their size and connectivity. It also aims to show a comprehensive methodology to characterise fracture networks by the use of geometrical and topological attributes of fractures at different scales of observation (outcrop, airborne LiDAR, seismic).

2 Study areas and geological settings

2.1 Cariatiz carbonate platform, SE Spain

At outcrop, the focus of this study is on the Messinian carbonate platform of Cariatiz, which constitutes one of the pre-evaporitic Messinian sedimentary units in the Sorbas Basin (Martín and Braga, 1994; Braga and Martín, 1996). The Cariatiz platform is located on the northern margin of the Sorbas Basin, close to the village of Los Alías, SE Spain (Fig. 1). The Sorbas Basin is oriented E-W and it is bordered by the Sierra de los Filabres to the north and the Sierras Alhamilla and Cabrera to the south (Braga and Martín, 1996; Cuevas Castell et al., 2007; Reolid et al., 2014; Nooitgedacht et al., 2018) (Fig. 1b). The formation of this Neogene basin is linked to strike-slip (Jonk and Biermann, 2002) and extensional tectonism (Meijninger and Vissers, 2006), comprising strata of Middle Miocene to Quaternary ages (Martín and Braga, 1994; Reolid et al., 2014; Nooitgedacht et al., 2018). The geometry and stratigraphy of the Cariatiz Fringing Reef Unit have been subject of extensive research (Riding et al., 1991; Martín and Braga, 1994; Braga and Martín, 1996; Cuevas Castell et al., 2007; Sánchez-Almazo et al., 2007; Reolid et al., 2014; Nooitgedacht et al., 2018).

The Cariatiz Fringing Reef Unit was chosen in this work because of its unique three-dimensional exposure in which several fracture types with various sizes are recognised at different scales (Fig. 4). During platform development, the Sorbas Basin was affected by a regional tectonic uplift with a rate of *ca* 110 m/Myr, imposing a 3° dip to the Cariatiz platform. Different reef growth phases appear as clinoform bodies (Reolid et al., 2014) which, in addition to syn-depositional erosion, influenced the geometry of the platform (Cuevas Castell et al., 2007). Sea-level changes have been reported as the governing mechanism controlling carbonate productivity, reef slope geometry and stacking patterns of the clinoform bodies (Kendall and Schlager, 1981; Braga and Martín, 1996; Reolid et al., 2014).

The Messinian Fringing Reef Unit comprises six distinct depositional facies (Riding et al., 1991; Braga and Martín, 1996) (Fig. 4d). From the platform interior to the basin, these depositional facies are as follows:

1. Lagoon – parallel beds of calcarenites and calcirudites with abundant gastropods, red coralline algae, foraminifera, and mollusc remains. Small coral patches of *Porites* occur near the reef crest. Siliciclastic grains are locally mixed with carbonate sediments. Lagoonal beds dip 3° to the southwest (N216°E).
2. Reef framework – a 20 m thick unit subdivided into three sub-facies from top to bottom:

a. Reef crest zone (4-0 m water depth) – laminar to contorted *Porites* colonies with stromatolitic crusts. Contains rudstones with echinoderms and molluscs fill cavities.

b. Thicket zone (ca 4-10 m below the reef crest) – vertical corals and continuous lateral coral growth.

c. Lower pinnacle zone (ca 10-15 m below the reef crest) – pinnacle morphologies formed by columnar *Porites* connected by vertical and laminar coral growth (Fig. 4e). Bioclastic matrix fills in remaining spaces.

3. Reef talus slope (uppermost slope) – deposits of reef framework blocks and coral breccia with *Halimeda*, bivalves, molluscs, serpulids and coralline algae. Laminar *Porites* colonies encrusting bioclasts are frequent.
4. Proximal slope (middle slope) – well-bedded deep water calcarenites and calcirudites with bioclasts of serpulids, coralline algae, molluscs and abundant *Halimeda*.
5. Distal slope (lowermost slope) and basin – calcarenites, silty and sandy marls variably intercalated with basinal marls and diatomites (upper part of the Abad Member).
6. Fan delta – episodic flows of fan delta sediments during carbonate platform growth, alternating with conglomerates and sandstones intervals that interfinger with the carbonate platform.

2.2 Pernambuco carbonate platform, East Brazil

At the seismic scale, our study focuses on the Pernambuco carbonate platform, which is part of the eastern portion of the Brazilian continental platform, an area of stretched continental crust forming the Pernambuco Plateau (Magalhães et al., 2014; Buarque et al., 2017) (Fig. 2). The Pernambuco Basin is part of the Borborema Province, consisting of a complex collage of continental masses (dos Santos et al., 2010; Buarque et al., 2017). This province was subject of a series of Precambrian orogenic events, prior to late Mesozoic rifting stages that culminated in continental breakup during the Cretaceous (Darros de Matos, 1999; dos Santos et al., 2010; Buarque et al., 2017). The evolution of the basin was initially controlled by NE-SW and E-W Precambrian shear zones that were then reactivated during rifting as strike-slip and normal faults (Buarque et al., 2017). After that, the basin was controlled by NW-SE oblique transfer faults, in addition to N-S, WNW-ESE and NNW-SSE normal faults, during the Aptian-Albian (Buarque et al., 2017).

Buarque et al (2017) recognised five seismic sequences offshore Pernambuco. Seismic Sequence 1 represents the beginning of a sag phase, comprising Aptian-Albian rift strata and a salt layer. Salt layers generated large halokinetic features, such as diapirs and salt domes that cross-cut Seismic Sequence 2, a unit composed of Cenomanian-Santonian post-rift strata (Buarque et al., 2016, 2017, Fig. 7). Offshore carbonate deposition developed during two main post-rift intervals: the Cretaceous post-rift Seismic Sequence 3 during the Campanian-Maastrichtian, and the Lower Cenozoic post-rift Seismic Sequence 4 from Paleogene to Middle Miocene. Upper Miocene to Recent strata occur in Seismic Sequence 5, described as an Upper Cenozoic post-rift interval (Buarque et al., 2017 Figs. 4 and 5).

Sequences 3 and 4 comprise the Pernambuco carbonate platform (Fig. 2c). This platform was chosen because of its distinctive km-long normal faults located along the platform margin and platform interior, revealing a similar setting to the fractures observed on the platform margin in Cariatiz, but at a larger scale (Fig. 2b and c). In addition, seismic characteristics (geometries and seismic facies) observed in Pernambuco present similarities to the depositional facies in Cariatiz (Fig. 2c). Four seismic facies are recognised in Pernambuco from the platform interior to the basin:

1. Platform interior (lagoon) – semi-continuous to discontinuous, low- to medium-amplitude internal reflections capped by a high-amplitude reflector.

2. Reef framework – semi-continuous sub parallel reflections bounded by the platform margin, which coincides with a steep high-amplitude reflector.
3. Talus slope – chaotic, steep reflections with low- to medium- amplitude.
4. Slope and basin (including the proximal and distal slopes) – discontinuous, chaotic reflections with low- to medium- amplitude.

3 Methods and datasets

Outcrop data from the Cariatiz carbonate platform are interpreted in this study, including ten sampling sites and airborne LiDAR data covering an area of about 0.4 km^2 (Figs. 4, 5 and 6). Cariatiz is used as an outcrop analogue to understand the complexity of sub-seismic fracture networks as the platform displays a multi-scale system of fractures identified from airborne LiDAR maps down to the outcrop scale. The aim is to correlate fracture networks measured from both field datasets to investigate the relationship between small and intermediate scale of observations. In a later stage, a seismic dataset from the Pernambuco Basin in Brazil was used to analyse fracture networks at a large scale. The methodology used in this work is summarised in Fig. 3.

The main rationale behind the use of datasets from two different localities, and with varied resolutions, was to investigate the effects of scale when characterising multi-scale fracture networks. As observed from platform to basin transects of both platforms, seismic facies and geometries from Pernambuco relate to depositional and structural settings at Cariatiz (Figs. 2c and 4d). In addition, fractures are observed along the platform margin in both Pernambuco and Cariatiz platforms (Figs. 2c and 4d). Nevertheless, each dataset has a distinctive resolution in which a range of specific fracture sizes can be observed. Centimetre-long fractures can be measured from exposure outcrop mapping, whereas fractures with a few metres in length can be mapped from airborne LiDAR datasets, and kilometre fractures can be measured utilising seismic data. This approach allowed us to understand which geological features can be observed at each particular scale. Our analysis does not intend to suggest that both platforms have the same fracture network properties, as they have different tectonic histories. In fact, our results demonstrate the differences of fracture network properties obtained from the two localities. However, the use of outcrop data can help to understand the complexity of fracture networks at different scales of observation, and the amount of detail that is lost due to data resolution.

3.1 Topological sampling

A fracture network is defined as a system of fractures developed within the same volume of rock, and may include different fracture sets that could interact by connecting individual fractures (Adler and Thovert, 1999; Sanderson and Nixon, 2015). An important part of our workflow is to consider the topology of fracture networks from the three studied datasets. Topology is the tool that allows geoscientists to properly characterise the connectivity (and relationships) of a given fractured unit, in addition to geometrical attributes (Manzocchi, 2002; Sanderson and Nixon, 2018). A combined analysis of fracture networks is the best practice, as geometrical data on its own is not sufficient to produce a model reflecting the connectivity of a fractured rock volume. In fact, two fracture networks with the same geometrical properties (orientation, length) can show different connectivity (Sanderson and Nixon, 2018).

This work follows the models of Manzocchi (2002) and Sanderson and Nixon (2015) in which fracture networks are considered in terms of traces (lines) and nodes (fracture intersections and terminations) to form a system of branches between nodes (Fig. 7a). Fracture network topology is given by the analysis of node types (I: isolated, Y: abutting or splaying, X: crossing) and branch types (I-I: isolated, I-C: partly connected, CC: doubly connected). It also involves resulting dimensionless parameters such as average number of connections per line (C_L), average number of connections per branch (C_B), and dimensionless branch intensity at percolation (B_{22C}) (Manzocchi, 2002; Sanderson and Nixon, 2015, 2018) (Figs. 3 and 7a,

Table D1). In order to further differentiate fracture populations, nodal functions such as the N_B/N_L ratio, proportions of connecting nodes (isolated: P_I or connected: P_C) and branches (isolated: P_{II}, singly connected: P_{IC} or doubly connected: P_{CC}) are useful to our analysis (Table D1).

Topological data and resulting dimensionless parameters are analysed using a series of equations and diagrams from Sanderson and Nixon (2015, 2018) (Table D1). A simple approach to assess the topology and connectivity of fracture networks consists of plotting nodal and branch data in ternary plots (Manzocchi, 2002; Sanderson and Nixon, 2015; Morley and Nixon, 2016). Results from each dataset vary between outcrop locations, zones or depths. An area covering the data variability is shown in ternary diagrams in addition to their average values (Fig. 11). In this work, we used the Ternary Plot Maker (2019) to plot our data.

As suggested by Sanderson and Nixon (2015, 2018), dimensionless parameters such as C_B, are useful measures to assess the connectivity of a fracture network. Values of C_B range from 0-2. On a ternary diagram, low connected networks with C_B values close to 0, plot towards the I-I corner, whereas high connected networks with C_B close to 2, plot towards the C-C corner with a high proportion of interconnected branches. Furthermore, C_B can be used with B_{22C} to estimate the percolation threshold of a given network topology. Sanderson and Nixon (2018) demonstrated that most percolating systems have values of C_B>1.56.

3.2 Geometrical sampling

Geometric parameters considered in this study are branch lengths and branch orientations (strike), as they can be measured at different scales from the three provided datasets. Sanderson and Nixon (2015, 2018) suggested that using branches instead of full traces is a better approach to characterise fracture networks as it can avoid or decrease sampling errors (Fig. 7 b-f). These errors can be related to (1) erroneous recognition, (2) censoring effects, and (3) truncation effects (Manzocchi et al., 2009; Guerriero et al., 2010; Torabi and Berg, 2011 2011; Tao and Alves, 2019).

Due to the complexity of fracture arrangements and the access limitation to entire fracture networks (censoring), it is a challenging task to define the full fracture trace (Fig. 7b). Erroneous recognition of the full fracture trace is common among interpreters as length and orientation measurements of fracture traces may differ between different interpretations (Fig. 7b). Variations in the results (e.g. orientation and length) between interpreters can lead to distinct and contrasting conclusions about a given fracture network. Identifying shorter segments (branches) during interpretation is a consistent protocol to measure fracture geometries (Fig. 7c). Results obtained utilising fracture branches can lead to similarities between interpreters, avoiding the erroneous recognition bias, as the identification of the full trace is not required.

Furthermore, censoring effects occur when a fracture extends beyond the sampling area and the frequency of large fractures is underestimated (Fig. 7e). This effect can be reduced by the use of fracture branches as the segment outside the sampling area is shorter (Fig. 7f). On the other hand, truncation effects occur when small fracture frequencies are underestimated as a result of resolution limitations that cannot be avoided due to data constraints (Fig. 7d). Therefore, we stress the use of fracture branches in all measurements collected in this paper as the obtained values can decrease uncertainties related to fracture sampling and provide more reliable information about the geometrical parameters (length and orientation) (Fig. 7).

3.3 Cariatiz Platform

3.3.1 Outcrop data – Field procedure

Geometrical and topological attributes were measured from the Cariatiz reef framework zone (Fig. 4a, d) on 10 outcrop surfaces (a 2D view of a fracture network) using the enhanced circular scanline methodology of Watkins *et al.* (2015) (Fig. 5). More than 400 fracture traces with ~1000 fracture branches were measured and analysed (Fig. 5). Topological analyses and field procedures are similar to Sanderson and Nixon (2015) and Procter and Sanderson (2018) in which we defined nodes and branches in the field and used rectified outcrop photographs (Figs. 3, 5 and 7).

The first stage in our workflow was to select key sampling localities prior to fracture data collection (Fig. 3). Sampling localities were initially chosen along the platform rim, within the reef framework facies, using aerial photographs and LiDAR maps with elevation and slope attributes (Fig. 6). This step was crucial to identify accessible areas where the fringing reef could be mapped along exposed outcrop surfaces. Field measurements were dependent on how clearly the fractures were exposed at the surface. Vegetation is preferentially localised within fractures, as these are zones of intense weathering where soil accumulates and moisture is retained, especially in arid conditions such as in Cariatiz (Boyer and McQueen, 1964; Aich and Gross, 2008). As a result, soil and vegetation was present at some localities, indicating the presence of open fractures (Fig. 5b, d). However, prior to fracture measurement, large vegetation was removed, and soil was cleared from the outcrop surface.

The circular scanline sampling method was used to count the number of fracture intersections at the edge of the circle (n) and the number of fracture terminations within the circle (m) (Mauldon et al., 2001; Watkins et al., 2015) (Figs. 3 and 5). At each sampling locality, a circle of known radius was drawn onto the surface using a length of rope with a stick of chalk tied to the end (Figs. 3 and 5). The radius was chosen based on the minimum m and n count (30) of Rohrbaugh *et al.* (2002) and Watkins *et al.* (2015) to ensure reliable fracture estimates and identify individual fracture sets or data clusters (Fig. 3). Following the method of Procter and Sanderson (2018), every node and branch was marked with chalk of different colours, depending on their type, to help node and branch counting. A sketch of the fracture network was drawn on the go to provide robust documentation of the measured data and to guide digital interpretation at a later stage.

Once fracture nodes and branches were identified within the sampling circle, geometrical measurements were performed in the field. The workflow included measuring fracture branch orientation (strike, dip and dip direction), branch length, as well as identifying aperture and fracture fill. By completion of topological and geometrical measurements, a photograph of the locality was taken for a later use. Outcrop photographs of the circular scanline were rectified using the graphics suite of CorelDraw and Corel PaintShop Pro in order to remove distortions in 3D perspective (Fig. 5k, l). This process allows fracture attributes (branches, nodes) to be digitised as a vector graphic image, in order to provide a clear representation to scale of the outcrop fracture networks (Procter and Sanderson, 2018) (Fig. 5). Topological and geometrical attributes were also measured digitally using the vector lineaments to confirm the values taken in the field (Fig. 5). This process provides a good quality control of the measured data. Additionally, vector lineaments allow accurate calculations of average orientations and exact length measurements of irregular fracture branches. These latter measurements were the ones used in the subsequent statistical analyses.

3.3.2 LiDAR data – GIS analysis

Airborne LiDAR imagery from the Cariatiz carbonate platform permitted the collection of fracture measurements at an intermediate scale. Data was provided by the Instituto Geográfico Nacional (IGN) and the Centro Nacional de Información (CNIG) of Spain (Fig. 6). The airborne LiDAR map was acquired with a density of 0.5 points/m^2 with a 5 m grid size. After processing for slope, a resolution of about 5 m is suggested for the airborne LiDAR dataset. As a result, fractures of less than 5 m (below the LiDAR resolution) are subject to truncation effects. Fracture branches ranging from a few metres to tens of metres in length can be resolved from this dataset.

Visualisation and interpretation were carried out using ArcGIS 10.5. A slope attribute was calculated from the LiDAR map to highlight intermediate-scale discontinuities (fractures and fracture swarms) at Cariatiz (Fig. 6). A 3D visualisation of the LiDAR map, the slope attribute map and aerial photographs were used simultaneously in our fracture interpretation to be confident that the lineaments were real geological fractures and no other elements such as footpaths or agriculture terraces related to abandoned olive fields (Fig. 6). The LIDAR map was divided into three zones in order to understand spatial fracture variability in Cariatiz (Fig. 6b).

Each fracture branch was digitised as a single polyline to preserve geometrical characteristics such as fracture branch length and orientation. Guidance from Nyberg et al (2018) was used during the interpretation of fracture branches to avoid topological inconsistencies such as erroneous short isolated fracture branches or overlapping fracture branches. The snapping tool from GIS was crucial in this task. Node counting was performed by digitising points at fracture terminations (I-nodes) or fracture intersections (Y-, X-nodes). Geometrical attributes (length and orientation) were calculated using the "linear directional mean" tool from the "spatial statistics tools" in ArcGIS.

3.4 Pernambuco carbonate platform

3.4.1 Seismic data

A post-stack depth-converted 3D seismic volume from the Pernambuco Plateau, offshore East Brazil, was used in this study (Fig. 2). The seismic volume covers an area of 3,200 km^2 with a vertical penetration of almost 9 km. The seismic volume was provided by CGG and comprises 2700 inlines (IL) and 1899 crosslines (XL) with a 25 x 25 m line spacing and a vertical sampling interval of 5 m. The interpreted seismic data is in depth domain with SEG's American polarity, and of good quality, allowing for the detailed analysis of fracture networks on the wide platform margin (Fig. 8). There are no exploration wells in the study area.

Seismic attribute calculation and fracture interpretation were completed using Schlumberger Petrel®. A variance cube was computed for the entire Pernambuco seismic volume to compare the similarity of traces and highlight seismic discontinuities such as faults and fractures (Chopra and Marfurt, 2007; Brown, 2011; Marfurt and Alves, 2015) (Figs. 3 and 8). Eleven depth slices were analysed and interpreted from Z= -1020 to -2020 m at intervals of 100 m (Figs. 3 and 8). Fault interpretation was performed on a portion of the Pernambuco carbonate platform covering the shelf and slope. Faults were interpreted by visualising depth slices and seismic sections simultaneously to make sure that lineaments are real faults with a vertical displacement and avoid interpretation of artefacts (Fig. 2c). Data was then exported to Esri® ArcGIS Desktop where geometrical (branch length, orientation) and topological (nodal and branch counting) analyses were performed using the same methodology as with LiDAR data (Figs. 3 and 8).

3.5 Statistics and data analyses

A common practice to analyse geometrical attributes of a fracture network is to use rose diagrams and frequency distribution plots such as histograms and cumulative plots (Watterson et al., 1996; Odling, 1997; Nyberg et al., 2018). The geometrical data in this work is analysed by equal area rose diagrams and branch length-frequency plots. Branch length measurements were processed using Microsoft Excel, where histograms, box plots, a series of cumulative frequency plots, and tables with statistical data were compiled in order to identify distribution trends (negative exponential, log-normal or power law) in a similar way to Nyberg et al. (2018) (Fig. 9).

Fracture orientation measurements were processed using the Matlab® version of MARD 1.0 by Munro and Blenkinsop (2012). Rose diagrams were plotted using a bi-directional function with a weighted moving average and equal area. The weighting factor for all plots was

0.9 with a 9° aperture angle for data averaging (Figs. 10 a-c, B1 and B2). Visual analyses from these rose diagrams suggest that our data is multimodal with different fracture sets (Fig. 10).

Numerical techniques were key in our workflow to define specific fracture sets. Multimodal orientation datasets were divided into clusters utilising the cluster analysis tool in Orient 3.11.1 (Vollmer, 1990, 1995, 2015) (Fig. 10 d-f). The cluster analysis method included axial data in which the number of clusters (from 2 to 9) is defined by the user. Every data sample was tested using different number of clusters in which the dominant sets were mostly defined regardless of the cluster counts. Visual interpretation of fracture sets based on equal area rose diagrams (Fig. 10 a-c) was useful in determining the final selection of the number of clusters (Fig. 10 a-c). For every fracture set, the axial mean was calculated using the Statistics Tool within Orient 3.11.1.

4 Results – Fracture network characterisation

4.1 Fracture complexity

In this study, we recognised different fracture types depending on the scale of observation. At outcrop scale, fracture compartmentalisation, chaotic and curved stylolite surfaces, as well as vertical *Porites* on the platform edge, show how complex the structural and depositional attributes are on carbonate platforms like Cariatiz (Figs. 4 and 5). Open fractures (joints) and veins were recognised across the Cariatiz Reef Unit (Figs. 4 and 5g, h). Veins have calcite infill and can be observed in many of the circular scanlines analysed (Fig. 5g). Large vertical fractures are visible across the reef framework zone, extending from the reef crest down to the slope facies zone (Fig. 4a). These fractures create blocks and are related to slope instability.

From airborne LiDAR imagery, the main structures comprise fracture swarms composed of clusters with closely spaced fractures. These fracture swarms are identified in the field (Fig.

4c) but can be better mapped and measured with slope attribute maps from airborne LiDAR data (Fig. 6). At the largest (seismic) scale of Pernambuco, normal faults are observed from different depth slices and profile sections (Fig. 8). These faults have variable throws ranging from a few tens of metres (reaching the data resolution) up to 300 m in some areas (Fig. 2c). These faults have regional and large-scale tectonic origins in contrast to those observed at outcrop.

4.2 Fracture network geometry

4.2.1 Fracture length

4.2.1.1 Cariatiz platform – Outcrop data

The length of fracture branches at Cariatiz displays a wide range of sizes (Figs. 9a, b and A1). However, every site has a similar distribution of fracture branch lengths with a positive skew (Fig. A1). Data gathered from the ten field sites also have a positive skew, showing that smaller fracture branches are the most abundant with centimetre lengths (Figs. 9a and A1). Higher frequencies are observed in fractures ranging from 9.4 cm to 33.8 cm with a medium value of 19.3 cm and a mean of 25 cm (Fig. 9b).

Sites A and C present a unimodal distribution with a positive skew. The dominant lengths are 3 to 25 cm (Fig. A1a, c). Fracture branch length at Sites B and I show a multimodal distribution (Fig. A1b, i). There are two dominant peaks with ranges of 3 to 13 cm and 31 to 41 cm (Fig. A1b, i). Sites D and G have a bimodal distribution with major fracture length frequencies ranging from 5 to 17 cm and 21 to 39 cm in length (Fig. A1d, g). Fracture distribution in Site E shows a large positive skew with the highest frequency observed in fractures ranging from 3 to 11 cm (Fig. A1e). Sites F and H present a major peak in fractures ranging from 9 to 21 cm in length (Fig. A1f, h). Site J has a positive skew distribution, with a highest peak representing fractures from 3 to 21 cm in length (Fig. A1j).

We plotted cumulative percentages of fracture branch lengths to determine if they fit a distribution trend such as negative exponential, log-normal or power-law distribution models (Figs. 9c, d, e). Outcrop data is best represented by a negative exponential or lognormal distribution (Fig. 9d). A deviation from this trend is observed for the longest branches due to truncation effects.

4.2.1.2 Cariatiz platform – LiDAR data

Airborne LiDAR imagery has a resolution of 5 m, implying that lineaments with sizes below this value, such as centimetre-long fracture branches mapped at outcrop (joints and veins), cannot be identified on the LiDAR map (Fig. 6). Instead, fracture swarms that are difficult to measure at outcrop (Fig. 4c), can be easily recognised and measured at this scale (Fig. 6). Areas that appear to be highly fractured at outcrop, such as Site C (Fig. 5c), appear as areas with no fractures on the LiDAR map (Fig. 6), a character related to the absence of fracture swarms in that section of the platform.

The study area was divided into three different zones in order to understand fracture variability along the platform margin (Fig. 6b). Fracture branch length at the LiDAR scale ranges from 1.4 to 47 m. Data present a positively skewed distribution, similar to outcrop data (Fig. 9f, g). The higher concentration of fracture branches is observed from 5 m to 11.8 m, with a median value of 7.4 m and a mean of 9.2 m (Fig. 9f, g). Zones 1 and 3 have a positively skewed histogram (Fig. A1k, m). The dominant fracture branch length ranges from 4 to 11 m. Zone 2 has more variability with a less positive skewed histogram and dominant fracture branch lengths ranging from 6 to 20 m (Fig. A1l).

Plots of cumulative percentage against fracture branch lengths display a similar pattern to the outcrop data, having the best fit with a negative exponential or log-normal distribution

(Figs. 9h, i, j). A power-law distribution is only representative with fracture branches longer than 10 m.

4.2.1.3 Pernambuco platform – Seismic data

Fractures (faults) in the range of hundreds of metres to a few kilometres predominate on seismic data from Pernambuco. These faults have throws ranging from a few metres up to 300 m (Fig. 2c). In Pernambuco, the highest fracture frequency is represented by features between 636 m to 1360 m with a median value of 926 m, and a mean of 1064 m (Fig. 9k, l). Due to its resolution, features that were observed in the field at the Cariatiz platform such as fracture swarms, joints and veins are not visible in seismic data.

Fracture branch length distribution from depth slices at Z=-1020 m and Z=-1220 show a positive unimodal skew. The major peak is observed with branch lengths of 300 to 700 m (Fig. A2a, c). At a depth of -1120 m, fracture branch lengths have a multimodal distribution with a concentration of fractures between 500 to 600 m. Fault lengths range from 200 m to 2500 m (Fig. A2b).

The variance slice at a depth of Z= -1320 m shows a multimodal distribution with length peaks at 700 m, 1100 m, 1400 m and 1700 m. Most of the data ranges from 200 m to 2600 m with a few outliers (Fig. A2d). At Z= -1420 m, a slight positive skew with unimodal distribution is observed (Fig. A2e). The dominant fracture branch length ranges from 600 m to 1200 m (Fig. A2e). Fracture branch length distribution at Z= -1520 m ranges from 300 m to 3100 m, with predominant fractures between 700 m to 1100 m (Fig. A2f). A unimodal distribution is recognised on the variance slices at Z= -1620m, -1720 m, -1820 m, -1920 m and -2020 m. Fracture branch lengths range from 300 m to 3500 m. At these depths, the dominant values range from 500 m to 1300 m. A positive skew with a long tail towards the larger values is observed in all histograms (Fig. A2g, h, i, j, k). A negative exponential or log-normal distribution plot displays a reasonable fit over most of the data range at seismic scale. A poor fit is observed in longer faults (Fig. 9m, n, o).

4.2.2 Fracture orientation

4.2.2.1 Cariatiz platform – Outcrop data

Fracture strike distributions from field measurements differ slightly from site to site with rose diagrams showing different orientations at each locality (Figs. 1c and B1). Data gathered from all localities display a multimodal distribution with fractures striking nearly in all directions with similar frequencies (Fig. 10a). However, four fracture sets are defined based on the cluster analysis (Fig. 10d). The first two sets strike NE and E-W with an axial mean of N51°E and S89°E, respectively. The third set strikes SE (S38°E) followed by a fourth set striking N-S (S11°W). The axial mean of fracture set 1 is almost parallel to the orientation of the Cariatiz platform margin (Fig. 10d).

Sites A and B contain fracture sets with a multimodal distribution (Figs. 1c and B1a, b). Three fracture sets with high frequency are recognised. The first one strikes NE, while the second and third sets strike NW. Site C and D exhibit three fracture sets; the highest frequency coincides with a SW strike, followed by E-W fractures and a set striking to the SSW (Figs. 1c and B1c, d). Outcrop surfaces at Sites E, F and G exhibit two main fracture sets: a first set with a NW strike, and a second set striking widely NE (Figs. 1c and B1e, f, g). Fractures at Site H exhibit three main fracture sets, with the most dominant striking NE. The second and third fracture sets strike to the WNW and to the NW (Figs. 1c and B1h). Fractures at Sites I and J show a dominant NE strike, followed by a NW strike (Figs. 1c and B1i, j).

4.2.2.2 Cariatiz platform – LiDAR data

The average orientation of the Cariatiz carbonate platform margin is N55°E, as observed from the aerial and LiDAR maps (Figs. 6 and 10b). Three fracture sets are recognised on

LiDAR data along the Cariatiz fringing reef (Fig. 10e). The dominant Set 1, with the highest frequency, strikes to the NE (N59°E), in a direction similar to the edge of the platform margin (Figs. 6, 10b and e, and B1k, l, m). The second and third minor fracture sets strike to the N-S (N02°W) and SE (S71°E), respectively. The second fracture set is recognised in the three zones, but it is more predominant in Zone 1 (Fig. B1k).

4.2.2.3 Pernambuco platform – Seismic data

The orientation of the Pernambuco carbonate platform margin is N50°E as observed from seismic depth slices (Figs. 2b and 10c). Cluster analysis of fault orientation data from the eleven depth slices reveal a major set of faults (Set 1) aligned NE (N48°E), a direction parallel to the platform edge (Fig. 10 c and f). Two minor fracture sets with lower frequencies, striking N-S and E-W, are also recognised with axial means of S09°E and S77°E, respectively (Fig. 10f).

From each depth of observation, data can be summarised as follows. Fractures at Z=-1020 m depth predominantly strike NW (Fig. B2b). Two secondary sets are also recognised with NE and NNW strikes. At depths of Z= -1120 m, -1220 m, -1320 m and -1420 m, there are similar fracture orientations with a dominant set striking to the NE, followed by two minor fracture sets striking NNW and WNW (Fig. B2c, d, e). A primary fracture set striking NE is recognised from Z= -1520 m to -2020 m (Fig. B2g, h, i, j, k, l).

4.3 Fracture network topology

4.3.1 Cariatiz platform – Outcrop data

Abutting or Y nodes are the dominant type of nodes at the outcropping Cariatiz platform. Nodal data change slightly at each locality, which is observed as a zone of variability on the ternary plots (Figs. 11a, C1a). Based on our average results, the proportion of isolated nodes (P_I) at outcrop is low with a value approaching 9%, whereas the proportion of connected nodes (P_C) is 91% (Table D2). At Cariatiz, from outcrop scale, branch classification shows that isolated branches (P_{II}) are only 0.8%. The highest proportions are related to connected branches with 8.3% being singly connected (P_{IC}) and 82.4% being doubly connected (P_{CC}) (Table D2). The N_B/N_L ratio ranges between 2 to 4, but most values lie around 3, suggesting that small scale-length fracture networks are dominated by abutting or splaying fracture terminations (Figs. 11b, C1b, Table D2).

From the connectivity analysis we determined that in Cariatiz, the average number of connections per line (C_L) ranges from 2 to 5, with 50% of the data ranging between 3 to 4 (Figs. 11c, C1c, Table D2). Moreover, 70% of the outcrop fractures at Cariatiz have a C_B value ranging between 1.8 to 2 (Figs. 11d, C1d, Table D2), suggesting that the fracture network is well connected, mostly by Y nodes. High values of C_B also indicate that fracture networks at Cariatiz are above the percolation threshold. The branch classification diagram plots values towards the C-C corner (Figs. 11e, C1e), stressing the high proportion of interconnected branches at Cariatiz, which can favour fluid flow.

Fracture networks from localities B, C and I are less connected than most data and are typical of multimodal joint networks (see Procter and Sanderson, 2018) (Fig. C1a). These localities have tree-like geometries based on the average degree <d> value from Sanderson et al (2019).

4.3.2 Cariatiz platform – LiDAR data

LiDAR data indicates that on average, 51% of the nodes are of type I and 47% are of type Y, with only 2% of X nodes (Figs. 11a, Table D2). It suggests that fracture connectivity at a metre-scale is not as developed as at the centimetre-scale. At an intermediate scale, the proportion of isolated nodes (P_I) is 25%, and connected nodes (P_C) is 75% (Table D2). Branch classification reveals that proportions of isolated branches (P_{II}) represent 6.5% of the network and singly connected branches (P_{IC}) comprise 19% of the network. Higher proportions relate to doubly connected branches (P_{CC}) with 55.5% (Table D2).

The N_B/N_L ratio has a value of 2, suggesting low proportions of connected branches at the metre-scale (Fig. 11b, Table D2). The average number of connections per line (C_L) and per branch (C_B) are also lower than at outcrop, with values of 2 and 1.5, respectively (Fig. 11c, d, Table D2). Despite the observed low values of branch connectivity, single and double connected branches dominate the fracture network at the metre scale (Fig. 11e, Table D2). These fracture networks are tree-like and multicomponent, which suggest that the fractures observed here are localised and therefore not part of a connected regional system (Sanderson et al., 2019).

4.3.3 Pernambuco platform – Seismic data

Fracture topology on the Pernambuco carbonate platform is represented on average, by 39% of I nodes, 54% of Y nodes and 7% of X nodes (Figs. 11a, C1g, Table D2). The average proportions of having isolated nodes (P_I) is 17%, and the proportion of connected nodes (P_C) is 83% (Table D2). These proportions are similar to Cariatiz, as the proportions of connected nodes are higher than isolated nodes (Table D2). Regarding proportions of branches in Pernambuco, the proportion of isolated branches (P_{II}) are 2.9% (P_{II}) followed by singly connected branches (P_{IC}) with 14%. Higher proportions are observed in doubly connected branches (P_{CC}) with 69.1% (Table D2).

The N_B/N_L ratio ranges from 2 to 3 (Fig. 11b, C1h, Table D2). The average number of connections per line (C_L) is 2.64, with a range between 2 and 3. The average number of connections per branch (C_B) has a wider range from 1.4 to 1.8 and a median value of 1.66, suggesting a moderate fracture connectivity at the seismic scale and networks close to the percolation threshold (C_B = 1.56) (Sanderson and Nixon, 2018) (Fig. 11c, d; C1j, l; Table D2).

Doubly connected branches dominate the fracture network at seismic scale (Fig. 11e, C1k, Table D2).

5 Discussion

5.1 Fracture attribute relationships at different scales

Previous studies have explored the idea of limitations due to data resolution and the effects of scale on the spatial arrangements of fault and fracture networks. For instance, studies such as Strijker et al. (2012) and Gutmanis et al. (2018) have examined the challenges of analysing sub-seismic fracture networks and the presence of an “intermediate” data gap between fractures observed from seismic and borehole datasets. Furthermore, extensive research including Odling (1997) and Watterson et al. (1996) have discussed scaling relationships of fracture networks and the uncertainties related to sampling effects. Pickering et al. (1997) and Nixon et al. (2012) have also suggested that resolution limitations of seismic data affect the estimation of fault network parameters such as connectivity, as this appears to change depending on the data resolution.

This paper aims to perform a multi-scale analysis to understand the inherent complexity of natural fracture networks, the existing differences at each scale and their scale dependency. A way to understand sub-seismic features is by using outcrop analogues. For this reason, we utilised exposure mapping and airborne LiDAR maps from the Cariatiz carbonate platform in SE Spain. In parallel, seismic datasets such as the one from the Pernambuco carbonate platform in Brazil are important to study km-long subsurface features. It is recognised from geometrical and topological analyses of fracture networks from Cariatiz that they have different attributes depending on the scale of observation, which may also be related to the distinct fracture types observed at each scale (Fig. 12).

5.1.1 Fracture geometry

5.1.1.1 Orientation

The Cariatiz carbonate platform margin is oriented N55°E (Fig. 10). Fracture branch orientation data differ between centimetre scale-length (outcrop) and metre scale-length (LiDAR) fractures. Rose diagrams from each dataset have different distributions, implying that fracture development may vary depending on scale (Fig. 10). Equal area rose diagrams demonstrate a multimodal distribution of fracture orientations at outcrop (Fig. 10 a and d). These fractures are specifically recognised as open joints and calcite filled veins (Figs. 5g, h and 12a). Numerical methods of cluster analysis helped us to divide the data into four fracture sets with similar frequencies (Fig. 10d). Fracture set 1 is important as it strikes parallel to the Cariatiz platform margin with an axial mean of N51°E (Fig. 10d).

At airborne LiDAR scale, the main lineaments comprise large fracture swarms that may be better related to gravitational instability at the edge of the platform margin (Figs. 4c, 6 and 12a). Small centimetre-length fractures identified from the outcrop exposure mapping are not visible at LiDAR scale due to limitations in resolution, as the smallest features identified are about 5 m in length (Figs. 6 and 9g). Furthermore, the orientation distribution and cluster analysis of fractures observed from airborne LiDAR data show a clear dominant fracture set striking NE-SW, with an axial mean of N59°E (Fig. 10e). The orientation of the Cariatiz platform margin (N55°E) is similar to the dominant fracture set 1 identified from LiDAR data (Fig. 10e), suggesting that intermediate scale-length fractures are dependent on the geometry of the platform (Figs. 6 and 10e).

The orientation of the Pernambuco platform margin is N50°E (Fig. 10f). Similarly to LiDAR data from the Cariatiz platform, the dominant fracture set recognised from the equal area rose diagrams and cluster analysis, is parallel to the platform margin with an axial mean of N48°E (Fig. 10c and f). This result suggests that fractures at intermediate and large scales, namely fracture swarms and kilometre faults respectively, are mainly controlled by the geometry of the platform margin (Figs. 8 and 10). Although there is a fracture set recognised at outcrop that also correlates to the Cariatiz platform margin, it is not the most dominant set at the cm scale. This suggests that at outcrop, fracture development is also highly controlled by other processes such as intense weathering, and the uplift of the platform, in addition to gravitational instability at the proximity of the platform edge.

5.1.1.2 Scale gap

Studies such as Strijker *et al.* (2012) have identified a scale gap between fractures resolved on seismic and borehole data. Outcrop data from this study are used to describe fractures that occur in this "intermediate" gap. Scale gaps are created by the limited resolution of the imaging methods, and resolution is given by the smallest feature that can be observed and measured in a specific dataset. We recognise that exposure mapping from outcrop data can be useful to identify joints and veins (Fig. 5g, h) covering three orders of magnitude with fracture branches ranging from 10^{-3} to 10^{0} m in length (Fig. 12a). Airborne LiDAR data can cover two orders of magnitude with fracture branches ranging from 10^{0} to 10^{2} m in length (Fig. 12a), with the main observed features being fracture swarms. Fracture branch length measurements from outcrop and LiDAR data at Cariatiz, show that the higher frequencies of branch lengths range from 10 to 34 cm and 5 to 12 m, respectively (Figs. 9b, g and 12).

Fracture lengths in both datasets are below seismic resolution. Even the less abundant and largest fracture branches recognised on LiDAR, which are part of the outliers of the data, have lengths of less than 50 m. Given a line spacing of 25 x 25 m on a seismic dataset, these fracture lengths would be subject to truncation effects and not visible from seismic data (Figs. 9g, d and 12). Moreover, the smallest fracture branch length recognised on seismic data is 100 m (Figs. 9k, l and 12). As a result, a scale gap in terms of fracture branch length is observed with no overlap between datasets (outcrop-LiDAR and LiDAR-seismic) due to the fact that resolution limits in the imaging methods constrain reliable fracture characterisation (Fig. 12a). A fundamental issue when measuring fractures from any source of data is the inherited limitation of the sampling bias due to censoring and truncation effects (Guerriero et al., 2010; Torabi and Berg, 2011 2011) (Fig. 7). These effects can cause under- or over- estimation of statistical parameters, compromising the results of fracture characterisation.

As observed in the field, fractures at the "transitional" scale do exist in nature, and the gap can be breached by the use of a dataset that can cover the resolution of those features. For instance, large vertical fractures are observed at the edge of the Cariatiz platform, creating compartmentalised blocks (Fig. 4a). Those fractures have high censoring effects at the outcrop scale as they extend outside the observable area, and at airborne LiDAR they are not identified due to truncation effects; therefore their presence is underestimated (Figs. 7d, e and 12a).

The Pernambuco seismic data is useful to understand features (faults) that one can encounter when analysing large carbonate platforms such as Pernambuco's, which is more than 40 km wide and hundreds of kilometres long (Fig. 2). From our analysis we determined that at this scale, fracture branches can be observed and measured with a range of 10^2 to 10^4 m in length (Fig. 12a). However, when comparing large carbonate platforms with smaller structures such as isolated carbonate platforms (ICPs), these latter have dimensions ranging from 2 to 18 km, such as those ICPs in the North West Shelf of Australia (Loza Espejel et al., 2019) and the South China Sea (Zampetti et al., 2004, Fig. 15). Internal fault branches within these structures are a few hundreds of metres long and cannot be fully resolved in seismic data. These types of faults would be part of the "transitional" gap that cannot be resolved by the use of datasets with comparable scales to either airborne LiDAR maps or seismic data (Fig. 12a). Only large, regional faults crossing the ICPs can be easily observed in seismic data. This is related to the size of the fractures as well as the seismic response in ICP facies. ICP facies are typically characterised by chaotic and low amplitude reflectors (Burgess et al., 2013; Loza Espejel et al., 2019). Any feature below this range is considered as sub-seismic and therefore additional data with higher resolution is required to be able to observe these faults (Fig. 12a).

The problem of scale gaps between datasets is partly related to the fact that, in all datasets, the highest frequency of fracture branch lengths is concentrated at the smaller lengths of each resolution, which is observed from histograms in the form of a positive skew distribution (Figs. 9). Even if there is a small overlap and fractures of similar length can be observed from two different scales of observation, those measurements are on the limit of the resolution of both datasets and therefore not representative due to censoring and truncation effects. The gap size will depend on the detail and parameters of the data acquisition for different datasets.

In order to obtain a better controlled model of the fracture network characterisation, it is critical to bridge those gaps and obtain datasets in which fracture observations considerably overlap from one dataset to another. This can be done by acquiring datasets with higher resolutions. For instance, to link outcrop observations with aerial LiDAR maps, high-resolution drone imagery or ground-based LiDAR mapping could be used (Fig. 12a). To link LiDAR and seismic datasets, changes to acquisition parameters of LiDAR maps and seismic volumes could be made to increase the data resolution; or if possible, an intermediate-scale high resolution seismic survey could be acquired to bridge the scale gap between the seismic and airborne LiDAR data (Fig. 12a). This is important, as higher resolution seismic data processed to image a certain depth (and frequency spectrum) can reveal fracture patterns that the original exploration surveys may not have imaged in the first place, as the original interest was to image the entire thickness of sediments on a basin.

5.1.1.3 Branch length

There has been much discussion on whether fracture trace length distributions are exponential or power-law (Needham et al., 1996; Nicol et al., 1996; Gillespie et al., 2001; Zeeb et al., 2013; Liu et al., 2016). Studies such as Gillespie *et al.* (2001) and Strijker *et al.* (2012) have analysed fracture trace length distributions from different datasets and concluded that for massive, non-stratabound units, fracture trace lengths can be represented by a power-law distribution, while stratabound units can be represented by a lognormal distribution. Despite the wide range of published work on trace length distribution, there seems to be a lack of knowledge in the literature about branch length distributions.

The Cariatiz platform has a complex geometry in which bedding cannot be observed at the reef framework; instead, massive rock units are intensely fractured to create large blocks and compartmentalise the carbonate unit (Fig. 4). Branch length analysis from outcrop and LiDAR data suggest that, for massive units like Cariatiz, a negative exponential distribution better represents the fracture distribution, with a deviation for longer trace lengths due to truncation effects (Fig. 12c). Such a trend can be expected to extend over longer fracture branches, as fracture distribution in Pernambuco with km-long fractures follows the same trend (negative exponential or log-normal distribution; see cumulative plot in Fig. 9n). This may suggest that, in order to predict smaller scale-length fracture branches when utilising seismic data, a negative exponential distribution can be used. This is of particular importance to reservoir characterisation in which prediction of sub-seismic fractures is key.

5.1.2 Fracture topology

Topology is a relevant aspect when characterising fracture networks as dimensionless parameters can be obtained to understand specific attributes such as connectivity (Sanderson, 2016; Sanderson and Nixon, 2018). Exposed outcrops on the Cariatiz carbonate platform allowed a detailed analysis of fracture network distribution (Fig. 11). Outcrop results show a variability cloud with an average of high proportions of connected nodes (mostly Y) and low proportions of isolated nodes. Conversely airborne LiDAR results demonstrate that larger fracture branches at Cariatiz have less connected nodes with an almost equal proportion of I and Y nodes (Figs. 11a, C1a and Table D2). The average number of connections per branch analysis (C_B) demonstrates that outcrop data are better connected than LiDAR data with an average of 1.8 and 1.5, respectively (Figs. 11d, C1d and Table D2).

Branch classification shows that outcrop scale fractures have high proportions of doubly connected branches and low proportions of singly connected branches with almost no isolated branches. LiDAR data is also dominated by doubly connected branches, but with lower proportions than the observed at outcrop as isolated branches have slightly higher proportions (Figs. 11e, C1e and Table D2). Branch classification thus suggests that smaller fractures have a higher probability to form connected branches (single and double) than larger fractures observed on the LiDAR map. This can be confirmed by the analysis of connections per branch and dimensionless intensity (Manzocchi, 2002; Sanderson and Nixon, 2018).

Sanderson and Nixon (2018) suggested that dimensionless parameters such as the average of connections per branch (C_B) and dimensionless branch intensity (B_{22C}) are useful measures of connectivity. These measures are also related to percolation in which systems with $C_B > 1.56$ can indicate percolation. Topological results from Cariatiz were plotted using Fig. 10d from Sanderson and Nixon (2018) (Fig. 11f). From this diagram it is observed that fractures at outcrop are mostly plotted above the percolation threshold, whereas fractures from the LiDAR data plot just below the percolation threshold. When comparing the higher values of C_B for outcrop data (C_B=1.8) with those obtained by LiDAR (C_B=1.5), the results suggest that small length scale fractures are better connected than intermediate length fractures (Fig. 11f). These results align with the observations from Nixon et al (2012, Fig. 14), suggesting that for carbonate platforms comparable to Cariatiz, fracture connectivity increases with increasing data resolution. Fault networks appear to be less connected at lower resolutions according to the latter authors.

If the connectivity trend recognised from outcrop and LiDAR continues towards larger fracture lengths, in a similar way to the trend observed by Nixon et al (2012, Fig. 14) as a function of data resolution, longer faults and fractures at Cariatiz, resolvable at seismic scale, would be expected to plot closer to the I node corner (Fig. 11d). These topological values expected at seismic scale would have lower values of C_B and therefore be less connected (Fig. 11d). This observation is important as it suggests that topological results at the largest scale analysed (e.g. seismic), are expected to have lower values of connectivity than fractures analysed at small scale (e.g. outcrop), given that connectivity may increase as the resolution increases and smaller fracture branches are measured. This trend is expected to occur in carbonate platforms with similar settings to Cariatiz, in which connectivity decreases as scale is increased. Further research is however needed in order to accurately predict the exact range of topological values at a different scale.

At seismic scale in Pernambuco the average proportions of connected nodes are considerably higher than the proportions of isolated nodes. Doubly connected branches have also higher proportions than singly connected and isolated branches. In Pernambuco, the average number of connections per branch (C_B) is 1.66 (Table D2) and, when analysed together with the dimensionless branch intensity at percolation (B_{22C}), it is observed that the values are on average, well connected and above the percolation threshold (Fig. 11l). As stated from the Cariatiz topological trend, topological results of large fracture branches from the Pernambuco carbonate platform analysed from seismic scale (large scale) are expected to have lower connectivity values than sub-seismic smaller fractures. Consequently, sub-seismic fractures in Pernambuco are expected to be better connected with values plotted closer to the Y node corner and higher values of C_B (Fig. 11j).

5.2 *Implications to naturally fractured reservoirs*

Fracture network characterisation plays an important role in hydrocarbon exploration and the development of naturally fractured reservoirs. It is known that the use of outcrop analogues is key to predict sub-seismic fracture networks, particularly when borehole data (e.g. well cores, image logs) are not available and there is the need to estimate the volume capacity and fluid flow of a given unit (Gutmanis et al., 2018). Outcrop analogues can provide valuable information on the behaviour of small (centimetre) and intermediate (metre) scale fracture networks by the combination of outcrop and LiDAR data, respectively. Predicting the geometry (orientation and length) and topology (dimensionless parameters) of fracture networks at sub-seismic scales is crucial to increase the quality of fracture network characterisation. The study from Cariatiz demonstrates that fracture networks at a smaller scale (e.g. outcrop) have a higher level of connectivity than in a larger scale (e.g. LiDAR) with higher values of C_B. We may predict that sub-seismic fractures have a better connectivity than seismic fractures. Topological parameters measured from seismic data represent lower values of connectivity compared to smaller fractures expected within the reservoir. Fracture network results obtained from fractures observed at seismic (km long) scale are not representative for the multi-scale fracture system, and only describe the parameters of km-long fracture branches. As a result, fracture reservoir models utilising topological parameters obtained from seismic fractures (km-long) may underestimate the presence of fractures at lower scales of observation. Areas that appear to have no faults on seismic data, might be highly fractured as observed in Cariatiz (Figs. 5 and 6). Consequently, a potential reservoir could be ignored if proper studies are not performed. To fully characterise the fracture system at different scales, including the reservoir, topological and geometrical analyses like those presented for Cariatiz and Pernambuco should be performed. Furthermore, negative exponential or log-normal distribution trends can be used to predict sub-seismic fracture branch lengths. It is advisable to use different resolution datasets such as borehole data and outcrop analogues to calibrate seismic results.

Open small-scale fracture networks mostly control the permeability characteristics of a rock, developing the main conduits of fluid flow (e.g. Bush, 2010; Questiaux et al., 2010). Conversely, when closed or cemented, they can provide barriers or baffles to fluid flow and contribute to reservoir compartmentalisation (Damsleth et al., 1998; Steen et al., 1998; Laubach, 2003; Maerten et al., 2006; Strijker et al., 2012). As suggested by Sanderson and Nixon (2018), topological values of C_B and B_{22C} are important to understand parameters such as permeability in a reservoir as they are related to connectivity and percolation. The permeability of a rock and resulting fluid flow are mainly dependent on the fracture network with topological values above the percolation threshold, assuming that fractures are conductive (Fig. 11f, l). In contrast, permeability is dependent on the matrix where connectivity is below the percolation threshold and fracture conductivity is lower than the matrix (Fig. 11f, l).

The analysis provided in this study is not limited to fractured reservoirs with hydrocarbon accumulations, as our results and methodology could also be applied to other geoscience disciplines such as geothermal reservoirs, hydrogeology, or carbon storage projects.

6 Conclusions

Carbonate platforms present complex multi-scale structural and sedimentological characteristics as observed in Cariatiz (Fig. 4). The integration of fieldwork data with outcrop exposure mapping and airborne LiDAR studies from Cariatiz, Spain, and 3D seismic data from Pernambuco, Brazil, allowed a better understanding of multi-scale fracture networks developed on carbonate platforms. These analyses reveal the complexity of fracture networks at different scales and are useful to predict sub-seismic fractures from seismic datasets that are widely used in industry. Fractures at each scale of observation behave differently, having different geometrical and topological characteristics.

a) This study presented an integrated geometrical (orientation and branch length) and topological (node, branch counting and dimensionless parameters) analysis of fracture networks using a methodology in which small-, intermediate- and large- scale datasets are combined.

b) Multi-scale fracture networks in carbonate platforms are complex; different fracture types are identified at each scale of observation. At small scale, cm-long joints and veins are mostly recognised (Fig. 12a). Fracture swarms are the dominant type observed from airborne LiDAR, whereas km-long faults prevail at seismic scale (Fig. 12a).

c) Transitional scale gaps of fracture branch lengths between three scales of observation (outcrop - airborne LiDAR, airborne LiDAR – seismic) are recognised. Fracture branch lengths with sizes falling in these “transitional” gaps cannot be resolved by the resolution of the analysed datasets. However, fractures of these lengths do exist in nature, although datasets such as drone imagery and higher resolution seismic are needed to bridge the gaps and allow fractures of all sizes to be measured (Fig. 12). This issue is related to censoring and truncation effects.

d) Fracture branch orientation at intermediate (airborne LiDAR) and large (seismic) scales appear to be controlled by the dominant orientation of the platform margin. Dominant fracture sets observed in Cariatiz and Pernambuco strike parallel to the edge of the platform margin. Fracture branches at outcrop scale (< 1 m) strike in almost all directions, suggesting that different processes control the development of small fractures (Fig. 10).

e) Fracture branch length distributions from Cariatiz and Pernambuco fit a negative exponential or log-normal distribution in a massive, non-stratabound unit (Fig. 12).

This trend may be useful to predict sub-seismic branch lengths when working with seismic datasets.

f) Fracture connectivity changes as a function of scale as it appears to decrease as fracture length is increased (Fig. 11). This work complements the conclusions proposed by Nixon et al (2012) in which they studied changes in connectivity at different resolutions. Small-scale fracture branches measured at outcrop present higher connectivity than larger fractures observed in LiDAR data. Fracture networks measured from seismic data may show lower connectivity values compared to smaller fractures expected at reservoir scale. This suggests that sub-seismic fracture networks mainly control the permeability and fluid flow in reservoirs that are dominated by open fractures or, instead, may develop barriers to fluid flow and contribute to reservoir compartmentalisation when fractures are closed or cemented.

g) Outcrop data are useful to investigate the complexity of fracture networks and fracture types that occur at sub-seismic scale. Understanding these sub-seismic parameters allow us to better characterise fractured reservoirs.

7 Acknowledgements

The work contained in this paper is part of a PhD research supported by the Mexican National Council of Science and Technology (CONACYT) and the hydrocarbon Secretariat of Energy (SENER). We are thankful to the AAPG Grants-in-Aid General Fund Award 2018 to cover fieldwork expenses. We would like to thank David Sanderson, an anonymous reviewer and editor Cees Passchier for their thoughtful and useful comments and criticisms that helped improve the manuscript. CGG is acknowledged for the provision of the Pernambuco 3D seismic volume. The seismic data images are proprietary to and provided courtesy of CGG. Schlumberger Petrel®, ESRI ArcGIS® and CorelDRAW® are also acknowledged for granting academic licenses to Cardiff's 3D Seismic Lab.

8 References

Abotalib, A.Z., Heggy, E., Scabbia, G., Mazzoni, A., 2019. Groundwater dynamics in fossil fractured carbonate aquifers in Eastern Arabian Peninsula: A preliminary investigation. Journal of Hydrology 571, 460–470.

Adler, P.M., Thovert, J.-F., 1999. Fractures and fracture networks. Springer Science & Business Media.

Alavian, S.A., Whitson, C.H., 2005. CO2 IOR Potential in Naturally Fractured Haft Kel Field, Iran. International Petroleum Technology Conference. International Petroleum Technology Conference.

Berkowitz, B., 2002. Characterizing flow and transport in fractured geological media: A review. Advances in Water Resources 25, 861–884.

Bertotti, G., Hardebol, N., Taal-van Koppen, J.K., Luthi, S.M., 2007. Toward a quantitative definition of mechanical units: New techniques and results from an outcropping deep-water turbidite succession (Tanqua-Karoo Basin, South Africa). AAPG Bulletin 91, 1085–1098.

Bonnet, E., Bour, B.O., Odling, N.E., Davy, P., Bour, O., Odling, N.E., Davy, P., Main, I., Cowie, P., Berkowitz, B., 2001. Scaling of fracture systems in geological media. Reviews of Geophysics 39, 347–383.

Bourbiaux, B., 2010. Fractured Reservoir Simulation: a Challenging and Rewarding Issue. Oil & Gas Science and Technology-Rev. IFP 65, 227–238.

Braga, J.C., Martín, J.M., 1996. Geometries of reef advance in response to relative sea-level changes in a Messinian (uppermost Miocene) fringing reef (Cariatiz reef, Sorbas Basin, SE Spain). Sedimentary Geology 107, 61–81.

Brown, A.R., 2011. AAPG Memoir 42. Interpretation of three-dimensional seismic data, Seventh. ed. Society of Exploration Geophysicists and American Association of Petroleum Geologists, Tulsa, Oklahoma, U.S.A.

Buarque, B. V., Barbosa, J.A., Magalhães, J.R.G., Cruz Oliveira, J.T., Filho, O.J.C., 2016. Post-rift volcanic structures of the Pernambuco Plateau, northeastern Brazil. Journal of South American Earth Sciences 70, 251–267.

Buarque, B. V, Barbosa, J.A., Oliveira, J.T.C., Magalhães, J.R.G., Correia, O.J., Varela Buarque, B., 2017. Carbonate Buildups in the Pernambuco Basin, NE Brazil. An Acad Bras Cienc 89, 841–857.

Burgess, P.M., Winefield, P., Minzoni, M., Elders, C., 2013. Methods for identification of isolated carbonate buildups from seismic reflection data. AAPG Bulletin 97, 1071–1098.

Bush, I., 2010. An integrated approach to fracture characterisation., Oil Review Middle East Issue Two 88–91.

Cacas, M.C., Daniel, J.M., Letouzey, J., 2001. Nested geological modelling of naturally fractured reservoirs. Petroleum Geoscience 7, S43–S52.

Chen, Y., Ma, G., Wang, H., 2018. Heat extraction mechanism in a geothermal reservoir with rough-walled fracture networks. International Journal of Heat and Mass Transfer 126, 1083–1093.

Chilès, J.-P., 2005. Stochastic modeling of natural fractured media: a review. Geostatistics Banff 2004. Springer, 285–294.

Chopra, S., Marfurt, K.J., 2007. Seismic attributes for prospect identification and reservoir characterization. Society of Exploration Geophysicists and European Association of Geoscientists and Engineers.

Cowie, P.A., Knipe, R.J., Main, I.G., 1996. Introduction to the special issue. Journal of Structural Geology 18, v–xi.

Cuevas Castell, J.M., Betzler, C., Rössler, J., Hüssner, H., Peinl, M., 2007. Integrating outcrop data and forward computer modelling to unravel the development of a Messinian carbonate platform in SE Spain (Sorbas Basin). Sedimentology 54, 423–441.

Damsleth, E., Sangolt, V., Aamodt, G., 1998. Sub-seismic Faults Can Seriously Affect Fluid Flow in the Njord Field off Western Norway - A Stochastic Fault Modeling Case Study. SPE Annual Technical Conference and Exhibition. Society of Petroleum Engineers.

Darros de Matos, R.M., 1999. History of the northeast Brazilian rift system: kinematic implications for the break-up between Brazil and West Africa. Geological Society, London, Special Publications 153, 55–73.

Dominguez, G.C., Fernando, S. V., Chilingarian, G. V., 1992. Chapter 12 Simulation of Carbonate Reservoirs. Developments in Petroleum Science 30, 543–588.

Doornenbal, J.C., Kombrink, H., Bouroullec, R., Dalman, R.A.F., De Bruin, G., Geel, C.R., Houben, A.J.P., Jaarsma, B., Juez-Larré, J., Kortekaas, M., Mijnlieff, H.F., Nelskamp, S., Pharaoh, T.C., Ten Veen, J.H., Ter Borgh, M., Van Ojik, K., Verreussel, R.M.C.H., Verweij, J.M., Vis, G.-J., 2019. New insights on subsurface energy resources in the Southern North Sea Basin area. Geological Society, London, Special Publications 494, SP494-2018–178.

dos Santos, E.J., Schmus, W.R. Van, Kozuch, M., Neves, B.B. de B., 2010. The Cariris Velhos tectonic event in Northeast Brazil. Journal of South American Earth Sciences 29, 61–76.

Eberli, G.P., Anselmetti, F.S., Betzler, C., Van Konijnenburg, J.H., Bernoulli, D., 2005. Carbonate platform to basin transitions on seismic data and in outcrops: Great Bahama Bank and the Maiella Platform margin, Italy. AAPG Memoir 207–250.

Friedman, M., 1975. Fracture in rock. Reviews of Geophysics 13, 352.

Galvis, N.E.B., 2018. Geomechanics, Fluid Dynamics and Well Testing, Applied to Naturally Fractured Carbonate Reservoirs: Extreme Naturally Fractured Reservoirs. Springer.

Gillespie, P.A., Walsh, J.J., Watterson, J., Bonson, C.G., Manzocchi, T., 2001. Scaling relationships of joint and vein arrays from The Burren, Co. Clare, Ireland. Journal of Structural Geology 23, 183–201.

Guerriero, V., Iannace, A., Mazzoli, S., Parente, M., Vitale, S., Giorgioni, M., 2010. Quantifying uncertainties in multi-scale studies of fractured reservoir analogues: Implemented statistical analysis of scan line data from carbonate rocks. Journal of Structural Geology 32, 1271–1278.

Gutmanis, J., Ardèvol i Oró, L., Díez-Canseco, D., Chebbihi, L., Awdal, A., Cook, A., 2018. Fracture analysis of outcrop analogues to support modelling of the subseismic domain in carbonate reservoirs, south-central Pyrenees. Geological Society, London, Special Publications 459, 139–156.

Gutmanis, J.C., Ardèvol i Oró, L., 2015. Application of Pyrenean Fractured Carbonate Outcrops for Subsurface Reservoir Characterisation. 77th EAGE Conference and Exhibition 2015.

Hermansen, H., Landa, G.., Sylte, J.., Thomas, L.., 2000. Experiences after 10 years of waterflooding the Ekofisk Field, Norway. Journal of Petroleum Science and Engineering

26, 11–18.

Jonk, R., Biermann, C., 2002. Deformation in Neogene sediments of the Sorbas and Vera Basins (SE Spain): constraints on simple-shear deformation and rigid body rotation along major strike-slip faults. Journal of Structural Geology 24, 963–977.

Kendall, C.G.S.C., Schlager, W., 1981. Carbonates and relative changes in sea level. Marine Geology 44, 181–212.

Key, S.C., Agarwal, B., Søiland, G. V., Nielsen, H.H., 1999. Ekofisk Field redevelopment: improved reservoir management through cross-discipline technology and integration of three dimensional models. Geological Society, London, Petroleum Geology Conference Series 5, 1147–1155.

Kim, Y.-S., Sanderson, D.J., 2005. The relationship between displacement and length of faults: a review. Earth-Science Reviews 68, 317–334.

Kleipool, L.M., de Jong, K., de Vaal, E.L., Reijmer, J.J.G., 2017. Seismic characterization of switching platform geometries and dominant carbonate producers (Miocene, Las Negras, Spain). In: Della Porta, G. (Ed.), Sedimentology 64, 1676–1707.

Laubach, S.E., 2003. Practical approaches to identifying sealed and open fractures. AAPG Bulletin 87, 561–579.

Laubach, S.E., Olson, J.E., Gross, M.R., 2009. Mechanical and fracture stratigraphy. AAPG Bulletin 93, 1413–1426.

Liu, R., Li, B., Jiang, Y., 2016. A fractal model based on a new governing equation of fluid flow in fractures for characterizing hydraulic properties of rock fracture networks. Computers and Geotechnics 75, 57–68.

Lohr, T., 2004. Prediction of sub-seismic faults and fractures - integration of 3D seismic data, 3D retro- deformation, and well data on an example of deformation around an inverted fault. Seismic and Sub-Seismic Deformation on Different Scales in the NW German Basin 35–48.

Loza Espejel, R., Alves, T.M.T.M., Blenkinsop, T.G.T.G., 2019. Distribution and growth styles of isolated carbonate platforms as a function of fault propagation. Marine and Petroleum Geology In Press, 484–507.

Maerten, L., Gillespie, P., Daniel, J.-M., 2006. Three-dimensional geomechanical modeling for constraint of subseismic fault simulation. AAPG Bulletin 90, 1337–1358.

Magalhães, J.R., Barbosa, J.A., Oliveira, J.T.C., Lima Filho, M.F., 2014. Characterization of the ocean-continent transition in the Paraíba basin and Natal platform region, NE Brazil. Revista Brasileira de Geofísica 32 (3), 481–496.

Mandujano, J.J., Khachaturov, R.V., Tolson, G., Duncan Keppie, J., 2005. Curvature analysis applied to the Cantarell structure, southern Gulf of Mexico: implications for hydrocarbon exploration. Computers & Geosciences 31, 641–647.

Manzocchi, T., 2002. The connectivity of two-dimensional networks of spatially correlated fractures. Water Resources Research 38, 1-1-1–20.

Manzocchi, T., Walsh, J.J., Bailey, W.R., 2009. Population scaling biases in map samples of power-law fault systems. Journal of Structural Geology 31, 1612–1626.

March, R., Doster, F., Geiger, S., 2018. Assessment of CO2 Storage Potential in Naturally Fractured Reservoirs With Dual-Porosity Models. Water Resources Research 54, 1650–1668.

Marfurt, K.J., Alves, T.M., 2015. Pitfalls and limitations in seismic attribute interpretation of tectonic features. Interpretation 3, SB5–SB15.

Martín, J., Braga, J.C., 1994. Messinian events in the Sorbas Basin in southeastern Spain and their implications in the recent history of the Mediterranean. Sedimentary Geology 90, 257–268.

Mauldon, M., Dunne, W.M., Rohrbaugh, M.B., 2001. Circular scanlines and circular windows: new tools for characterizing the geometry of fracture traces. Journal of Structural Geology 23, 247–258.

Medici, G., West, L.J., Banwart, S.A., 2019. Groundwater flow velocities in a fractured carbonate aquifer-type: Implications for contaminant transport. Journal of Contaminant Hydrology 222, 1–16.

Meijninger, B.M.L., Vissers, R.L.M., 2006. Miocene extensional basin development in the Betic Cordillera, SE Spain revealed through analysis of the Alhama de Murcia and Crevillente Faults. Basin Research 18, 547–571.

Morley, C.K., Nixon, C.W., 2016. Topological characteristics of simple and complex normal fault networks. Journal of Structural Geology 84, 68–84.

Munro, M.A., Blenkinsop, T.G., 2012. MARD-A moving average rose diagram application for the geosciences. Computers and Geosciences 49, 112–120.

Needham, T., Yielding, G., Fox, R., 1996. Fault population description and prediction using examples from the offshore U.K. Journal of Structural Geology 18, 155–167.

Nelson, R.A., 2001. Geologic analysis of naturally fractured reservoirs, 2nd Edition. Gulf Professional Pub.

Nicol, A., Walsh, J.J.J., Watterson, J., Gillespie, P.A.A., 1996. Fault size distributions - Are they really power-law? Journal of Structural Geology 18, 191–197.

Nixon, C.W., Sanderson, D.J., Bull, J.M., 2012. Analysis of a strike-slip fault network using high resolution multibeam bathymetry, offshore NW Devon U.K. Tectonophysics 541–543, 69–80.

Nooitgedacht, C.W., Kleipool, L.M., Andeweg, B., Reolid, J., Betzler, C., Lindhorst, S., Reijmer, J.J.G., 2018. New insights in the development of syn-depositional fractures in rimmed flat-topped carbonate platforms, Neogene carbonate complexes, Sorbas Basin, SE Spain. Basin Research 30, 596–612.

Nyberg, B., Nixon, C.W., Sanderson, D.J., 2018. NetworkGT: A GIS tool for geometric and topological analysis of two-dimensional fracture networks. Geosphere 14, 1618–1634.

Odling, N.E., 1997. Scaling and connectivity of joint systems in sandstones from western Norway. Journal of Structural Geology 19, 1257–1271.

Odling, N.E., Gillespie, P., Bourgine, B., Castaing, C., Chiles, J.P., Christensen, N.P., Fillion, E., Genter, A., Olsen, C., Thrane, L., Trice, R., Aarseth, E., Walsh, J.J., Watterson, J., 1999. Variations in fracture system geometry and their implications for fluid flow in fractures hydrocarbon reservoirs. Petroleum Geoscience 5, 373–384.

Peacock, D.C.P., Knipe, R.J., Sanderson, D.J., 2000. Glossary of normal faults. Journal of Structural Geology 22, 291–305.

Peacock, D.C.P., Nixon, C.W., Rotevatn, A., Sanderson, D.J., Zuluaga, L.F., 2016. Glossary of fault and other fracture networks. Journal of Structural Geology 92, 12–29.

Pickering, G., Peacock, D.C.P., Sanderson, D.J., Bull, J.M., 1997. Modeling tip zones to predict the throw and length characteristics of faults. AAPG Bulletin 81, 82–99.

Procter, A., Sanderson, D.J., 2018. Spatial and layer-controlled variability in fracture networks. Journal of Structural Geology 108, 52–65.

Questiaux, J.-M., Couples, G.D., Ruby, N., 2010. Fractured reservoirs with fracture corridors. Geophysical Prospecting 58, 279–295.

Reolid, J., Betzler, C., Braga, J.C., Martín, J.M., Lindhorst, S., Reijmer, J.J.G., 2014. Reef slope geometries and facies distribution: controlling factors (Messinian, SE Spain). Facies 60, 737–753.

Riding, R., Martin, J.M., Braga, J.C., 1991. Coral-stromatolite reef framework, Upper Miocene, Almeria, Spain. Sedimentology 38, 799–818.

Rohrbaugh, M.B., Dunne, W.M., Mauldon, M., 2002. Estimating fracture trace intensity, density, and mean length using circular scan lines and windows. AAPG Bulletin 86, 2089–2104.

Sánchez-Almazo, I.M., Braga, J.C., Dinarès-Turell, J., Martín, J.M., Spiro, B., 2007. Palaeoceanographic controls on reef deposition: the Messinian Cariatiz reef (Sorbas Basin, Almería, SE Spain). Sedimentology 54, 637–660.

Sanderson, D.J., 2016. Field-based structural studies as analogues to sub-surface reservoirs. Geological Society, London, Special Publications 436, 207–217.

Sanderson, D.J., Nixon, C.W., 2018. Topology, connectivity and percolation in fracture networks. Journal of Structural Geology 115, 167–177.

Sanderson, D.J., Nixon, C.W., 2015. The use of topology in fracture network characterization.

Journal of Structural Geology 72, 55–66.

Sanderson, D.J., Peacock, D.C.P., Nixon, C.W., Rotevatn, A., 2019. Graph theory and the analysis of fracture networks. Journal of Structural Geology 125, 155–165.

Santiago, E., Velasco-Hernández, J.X., Romero-Salcedo, M., 2014. A methodology for the characterization of flow conductivity through the identification of communities in samples of fractured rocks. Expert Systems with Applications 41, 811–820.

Sarkheil, H., Hassani, H., Alinia, F., 2013. Fractures distribution modeling using fractal and multi-fractal–neural network analysis in Tabnak hydrocarbon field, Fars, Iran. Arabian Journal of Geosciences 6, 945–956.

Steen, Ø., Sverdrup, E., Hanssen, T.H., 1998. Predicting the distribution of small faults in a hydrocarbon reservoir by combining outcrop, seismic and well data. Geological Society, London, Special Publications 147, 27–50.

Strijker, G., Bertotti, G., Luthi, S.M., 2012. Multi-scale fracture network analysis from an outcrop analogue: A case study from the Cambro-Ordovician clastic succession in Petra, Jordan. Marine and Petroleum Geology 38, 104–116.

Tao, Z., Alves, T.M., 2019. Impacts of data sampling on the interpretation of normal fault propagation and segment linkage. Tectonophysics 762, 79–96.

TerHeege, J.H., Osinga, S., Carpentier, S., 2018. The Geomechanical Response of Naturally Fractured Carbonate Reservoirs to Operation of a Geothermal Doublet.

Torabi, A., Berg, S.S., 2011. Scaling of fault attributes: A review, Marine and Petroleum Geology. Elsevier.

Van As, A., Jeffrey, R.G., 2002. Hydraulic fracture growth in naturally fractured rock: mine through mapping and analysis.

Vidal, J., Genter, A., 2018. Overview of naturally permeable fractured reservoirs in the central and southern Upper Rhine Graben: Insights from geothermal wells. Geothermics 74, 57–73.

Vollmer, F.W., 2015. Orient 3: a new integrated software program for orientation data analysis, kinematic analysis, spherical projections, and Schmidt plots. Geological Society of America Abstracts with Programs. 49.

Vollmer, F.W., 1995. C program for automatic contouring of spherical orientation data using a modified Kamb method. Computers and Geosciences 21, 31–49.

Vollmer, F.W., 1990. An application of eigenvalue methods to structural domain analysis. GSA Bulletin 102, 786–791.

Watkins, H., Bond, C.E., Healy, D., Butler, R.W.H., 2015. Appraisal of fracture sampling methods and a new workflow to characterise heterogeneous fracture networks at outcrop. Journal of Structural Geology 72, 67–82.

Watterson, J., Walsh, J.J., Gillespie, P.A., Easton, S., 1996. Scaling systematics of fault sizes on a large-scale range fault map. Journal of Structural Geology 18, 199–214.

Zampetti, V., Schlager, W., van Konijnenburg, J.-H., Everts, A.-J., 2004. Architecture and growth history of a Miocene carbonate platform from 3D seismic reflection data; Luconia province, offshore Sarawak, Malaysia. Marine and Petroleum Geology 21, 517–534.

Zarei, H.R., Uromeihy, A., Sharifzadeh, M., 2012. Identifying geological hazards related to tunneling in carbonate karstic rocks - Zagros, Iran. Arabian Journal of Geosciences 5, 457–464.

Zeeb, C., Gomez-Rivas, E., Bons, P.D., Blum, P., 2013. Evaluation of Sampling methods for fracture network characterization using Outcrops. AAPG Bulletin 97, 1545–1566.

9 Figure captions

Figure 1. a) Location of the study area in SE Spain. b) Regional map of the Sorbas Basin showing the Messinian Reef Unit, and the area of interest at Cariatiz. Modified after Reolid et al. (2014). c) Topographic map showing the field sites where fracture network mapping was performed using the augmented circular scanline method of Watkins et al. (2015). Rose diagrams show the main fracture orientation at each site.

Figure 2. a) Location map of the study area in the Pernambuco Basin. b) Variance depth slice (-1720 m) showing the area (yellow line) where fracture characterisation was performed. c) Seismic section across the Pernambuco Platform showing its internal geometry and seismic facies, as well as the presence of normal faults. *Sequence numbers after Buarque et al (2017). Scale and exact location cannot be given due to data privacy.

Figure 3. Flowchart summarising the methodology used in this work to obtain fracture data from different datasets. Three different input datasets with distinct scale-resolution were utilised (outcrop: small scale, LiDAR: intermediate scale, seismic: large scale). *Consider suggestions by Rohrbaugh et al. (2002) and Watkins et al. (2015) to determine the radius (r). See more details in the text.

Figure 4. Outcrop images and facies model showing the complexity of structural and depositional attributes in the Cariatiz fringing reef unit. a) Outcrop image showing large fractures across the platform edge. b) Enlarged photo showing circular shapes of *Porites* on a horizontal section. c) Fracture swarms along the platform margin. See Fig. 6a for location. d) Facies model of Cariatiz, modified after Braga and Martín (1996) and Reolid et al. (Braga and Martín, 1996; Reolid et al., 2014). e) Outcrop photo showing vertical *Porites*. See Fig. 1c for location.

Figure 5. Rectified photographs of circular scanlines showing the fracture networks collected at outcrop in Cariatiz. a-j) Digitised fracture networks showing the topological parameters. Circular scanline (red line), fracture intersections with the sampling circle (yellow circle), I nodes (green triangles), Y nodes (blue squares), X nodes (orange hexagons). k) Field photograph showing the grid used to rectify the perspective of the circle. l) Rectified photo where geometrical and topological analyses can be performed.

Figure 6. LiDAR map of the study area in the Cariatiz carbonate platform with the slope attribute highlighting discontinuities. Fractures present high slope values. Site locations are shown with red circles. a) Uninterpreted 3D visualisation of the LiDAR map, useful to locate outcrop localities and perform fracture interpretation in the intermediate scale. b) Interpreted map showing fracture branches as black lines as well as fracture nodes. The map was divided into three zones to analyse fracture variability.

Figure 7. Schematic diagrams showing the topological analysis and sampling effects of fracture networks. a) Fracture traces (A-B and C-D) and their node and branch association with intersecting fractures (dashed lines). I-nodes (green circles); Y-nodes (blue triangles); X-nodes (orange diamonds); I-I or isolated branch (I-I nodes with no fracture intersection); I-C or partly connected branch (I-Y or I-X node intersection); and C-C or doubly connected branch (Y-Y, Y-X, or X-X node intersection). Modified from Sanderson and Nixon (2015). b) Erroneous recognition of fracture traces occurs as they can be interpreted differently depending on the criteria used, leading to inconsistent trace lengths and orientations depending on the interpreter. c) By utilising fracture branches as a result of topological analyses, the fracture segments can be identified easier, resulting in reliable measurements of geometrical characteristics. d) Truncation effects occur due to limits in data resolution, and it is present regardless of the use of branches or traces. e) Censoring effects occur as the fractures extend the observable area. f)

Censoring effects can be minimised by the use of fracture branches as they do not include the entire trace; rather only one segment of the trace.

Figure 8. Seismic depth slices of the Pernambuco carbonate shelf on the variance attribute computed in this work. Fracture interpretation was performed within an area of interest every 100 m in depth from Z=-1020 m to Z=-2020 m. Topological analyses were also carried out to better understand the fracture network. Fractures are represented with continuous pink lines. I nodes are represented by green triangles, Y nodes by blue squares, and X nodes by orange hexagons. Seismic images are rotated and therefore not in their original orientation due to data protection.

Figure 9. Statistical plots showing fracture branch length distribution from three scale datasets. Outcrop data from the Cariatiz carbonate platform is plotted in yellow. LiDAR data from the Cariatiz carbonate platform is plotted in green. Seismic data from the Pernambuco carbonate platform is plotted in blue. a), f) and k) Histograms showing a positive skew distribution. b), g) and l) Box plots showing the concentration of branch lengths. Q1, Q2 and Q3 are the values for the lower quartile, median and upper quartile. Box represents the interquartile range, thick solid grey line represents the minimum and maximum values (whiskers), and dotted line shows the outliers of the data. c), h) and m) Cumulative percentage plotted against fracture branch length; note good fit to a straight line for small branch lengths. d), i) and n) Log (cumulative percentage) plotted against fracture branch length, with straight line indicating negative exponential distribution. e), j) and o) Log (cumulative percentage) plotted against log (fracture branch length), with straight line indicating power-law distribution. Straight red line indicates a good fit.

Figure 10. Bi-directional moving average rose diagrams and numerical cluster analysis showing fracture orientation and fracture sets from (a and d) outcrop, (b and e) LiDAR, and (c

and f) seismic data. Rose diagrams were generated as equal area with a weighting factor of 0.9 and aperture of 9°. Equal area rose diagrams are used to visualise results from the cluster analyses.

Figure 11. Triangular plots showing detailed topological analyses of nodes and branches and resulting parameters from different scales of observation. a) to f) Outcrop and LiDAR topological results from the Cariatiz Fringing Reef Unit. g) to l) Seismic topological results from the Pernambuco carbonate platform. Yellow area represents the variation in results from outcrop data. Green area represents the variation in results from LiDAR maps. Similarly, blue area represents the variation in results from seismic data. *Purple area is an interpretation of topological values expected with branch lengths observable at seismic scale in Cariatiz. **Orange area is an interpretation of expected values at sub-seismic scale in Pernambuco assuming that fracture connectivity increases at a smaller scale, similarly to the observed trend in Cariatiz. a, g) Fracture network node classification. Yellow circle: average value from outcrop data; green triangle: average value from LiDAR data; and blue square: average value from seismic data. b, h) N_B/N_L ratio shows values of 3 for outcrop data, 2 for LiDAR data, and 2.5 for seismic data. c, i) Average number of connections per line (C_L) shows a value of 3.4 at outcrop level, a value of 2 from LiDAR data, and a value of 2.6 from seismic data. d, j) Average number of connections per branch (C_B) with a value of 1.82 at outcrop scale, 1.49 at LiDAR scale, and 1.66 at seismic scale. e, k) Branch classification with I-I isolated branches, I-C partly connected branches, and C-C doubly connected branches. f, l) Dimensionless intensity of branches at percolation (B_{22C}).

Figure 12. Multi-scale statistics of fracture branch lengths and figures showing different fracture types with associated datasets depending on scale. a) Outcrop photos with associated datasets and box plots showing the distribution of fracture branch lengths between different datasets. It is observed from the box plots that there is no overlap between datasets (outcrop -

airborne LiDAR and airborne LiDAR - seismic). Large fractures with a scale between outcrop and airborne LiDAR were recognised in the field and can be mapped with the use of ground LiDAR or drone imagery. Fractures observed at each scale are mainly of a different type. Veins and joints can be mapped at outcrop; fracture swarms can be mapped with airborne LiDAR maps; and large kilometre faults can be mapped by using seismic data. Fractures with a branch size in between the scale of the three studied datasets can be mapped with data of different resolution such as drone imagery and higher resolution seismic. b) Cumulative percentage plotted against fracture branch length; note good fit to a straight line for small branch lengths. c) Log (cumulative percentage) plotted against fracture branch length, with straight line indicating negative exponential distribution. d) Log (cumulative percentage) plotted against log (fracture branch length), with straight line indicating power-law distribution. Straight red line represents a good fit.

10 Appendices' captions

Figure A1. Fracture branch length histograms from the Cariatiz carbonate platform. a) to j) Histograms from outcrop localities. k) to m) Histograms from LiDAR zones.

Figure A2. Fracture branch length histograms from seismic data (depth slices -1020 m to -2020 m) in the Pernambuco carbonate platform. Fracture branches at seismic scale are in the range of hundreds of metres.

Figure B1. Bi-directional moving average rose diagrams showing fracture orientation from the Cariatiz carbonate platform. a) to j) Rose diagrams from outcrop localities. k) to m) Rose diagrams from LiDAR zones. Rose diagrams were generated as equal area with a weighting factor of 0.9 and aperture of 9°.

Figure B2. Bi-directional moving average rose diagrams showing fracture orientation from our study area in the Pernambuco carbonate platform at different seismic slices from Z=

-1020 m to -2020 m. Rose diagrams were generated as equal area with a weighting factor of 0.9 and aperture of 9°.

Figure C1. Triangular plots showing detailed topological analyses of nodes and branches from outcrop localities and LiDAR zones at the Cariatiz Fringing Reef (a to f), as well as seismic depth slices from the Pernambuco carbonate platform (g to l). Yellow, green and blue shapes represent the range of node and branch values at outcrop, LiDAR and seismic scale, respectively. a, g) Fracture network node classification. b, h) N_B/N_L ratio shows most of the points lying over N_B/N_L ratio value of 3 within the range of 2 and 4. c, i) Average number of connections per line (C_L) showing that in Cariatiz, at outcrop level, values range from 2 to 5. d, j) Average number of connections per branch (C_B). e, k) Branch classification with I-I isolated branches, I-C partly connected branches, and C-C doubly connected branches. f, l) Dimensionless intensity of branches (B_{22C}).

Table D1. Summary of topological parameters, notation, and key equations. Modified from Sanderson and Nixon (2015, 2018).

Table D2. Fracture topological results from field data (outcrop and LiDAR) and seismic data.

11 Figures

Figure 1

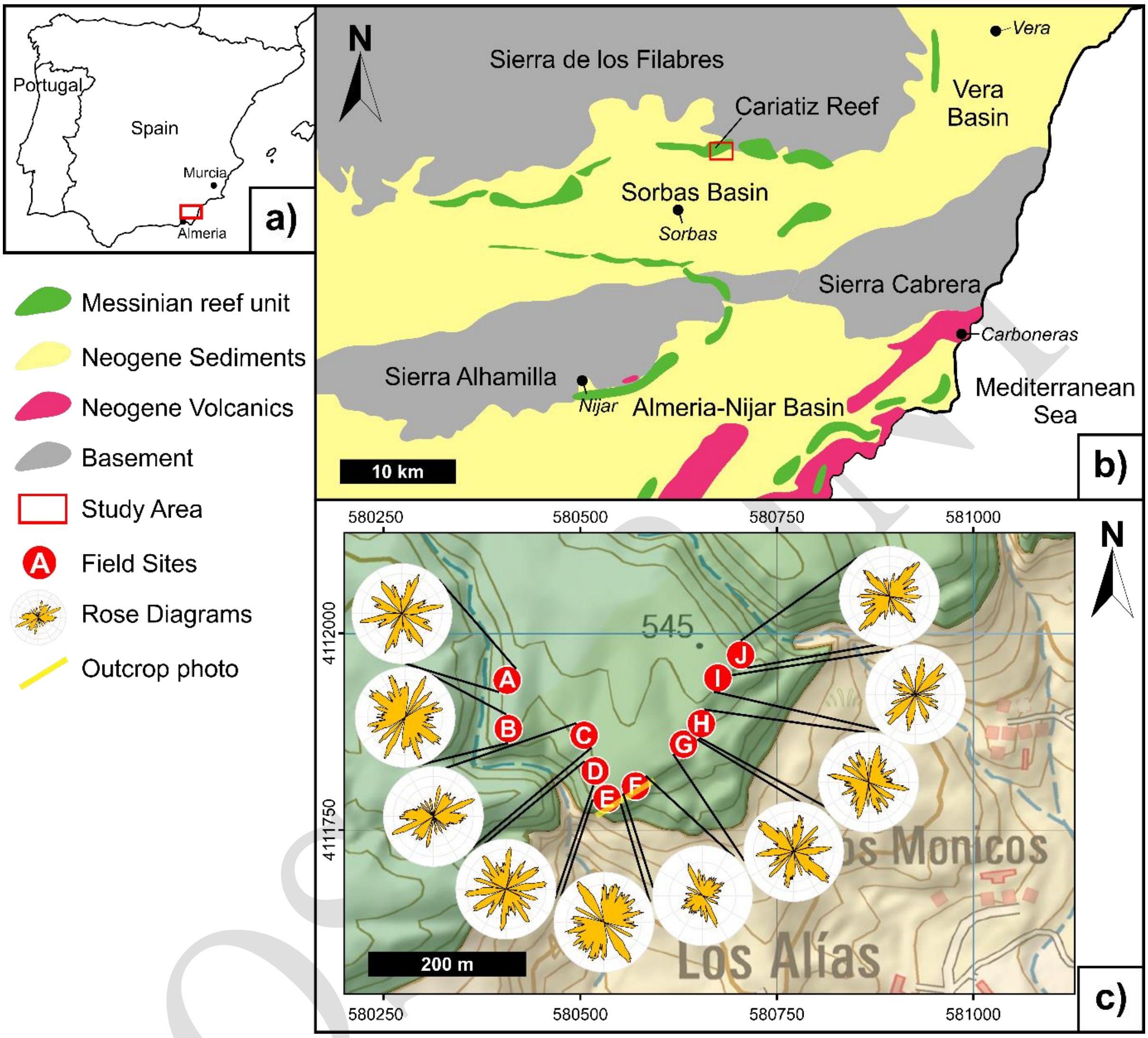

Figure 2

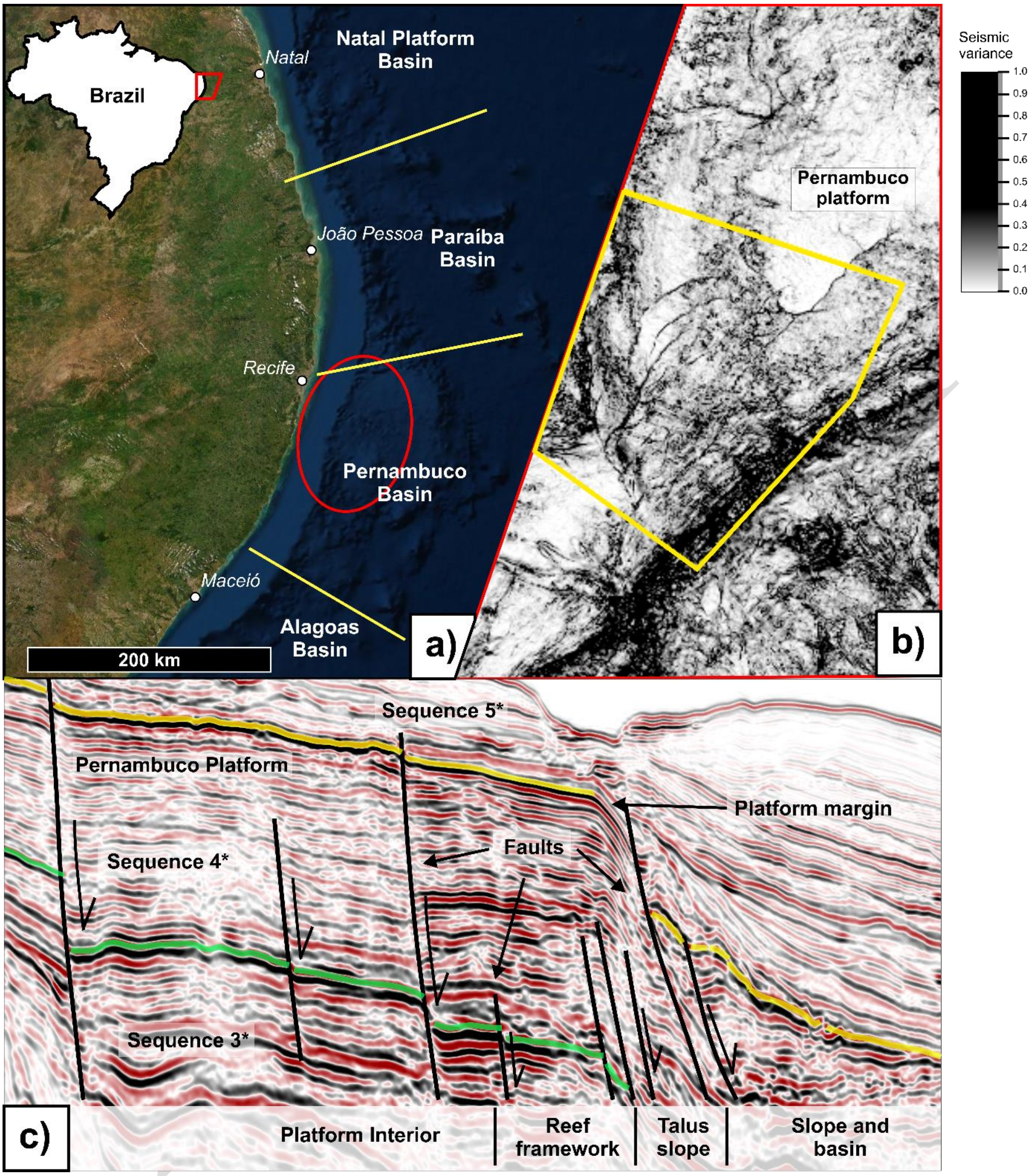
Seismic variance
1.0
0.9
0.8
0.7
0.6
0.5
0.4
0.3
0.2
0.1
0.0
Brazil
Natal
Natal Platform Basin
João Pessoa
Paraíba Basin
Recife
Pernambuco Basin
Maceió
Alagoas Basin
200 km
a)
Pernambuco platform
b)
Sequence 5*
Pernambuco Platform
Platform margin
Faults
Sequence 4*
Sequence 3*
c)
Platform Interior
Reef framework
Talus slope
Slope and basin

Figure 3

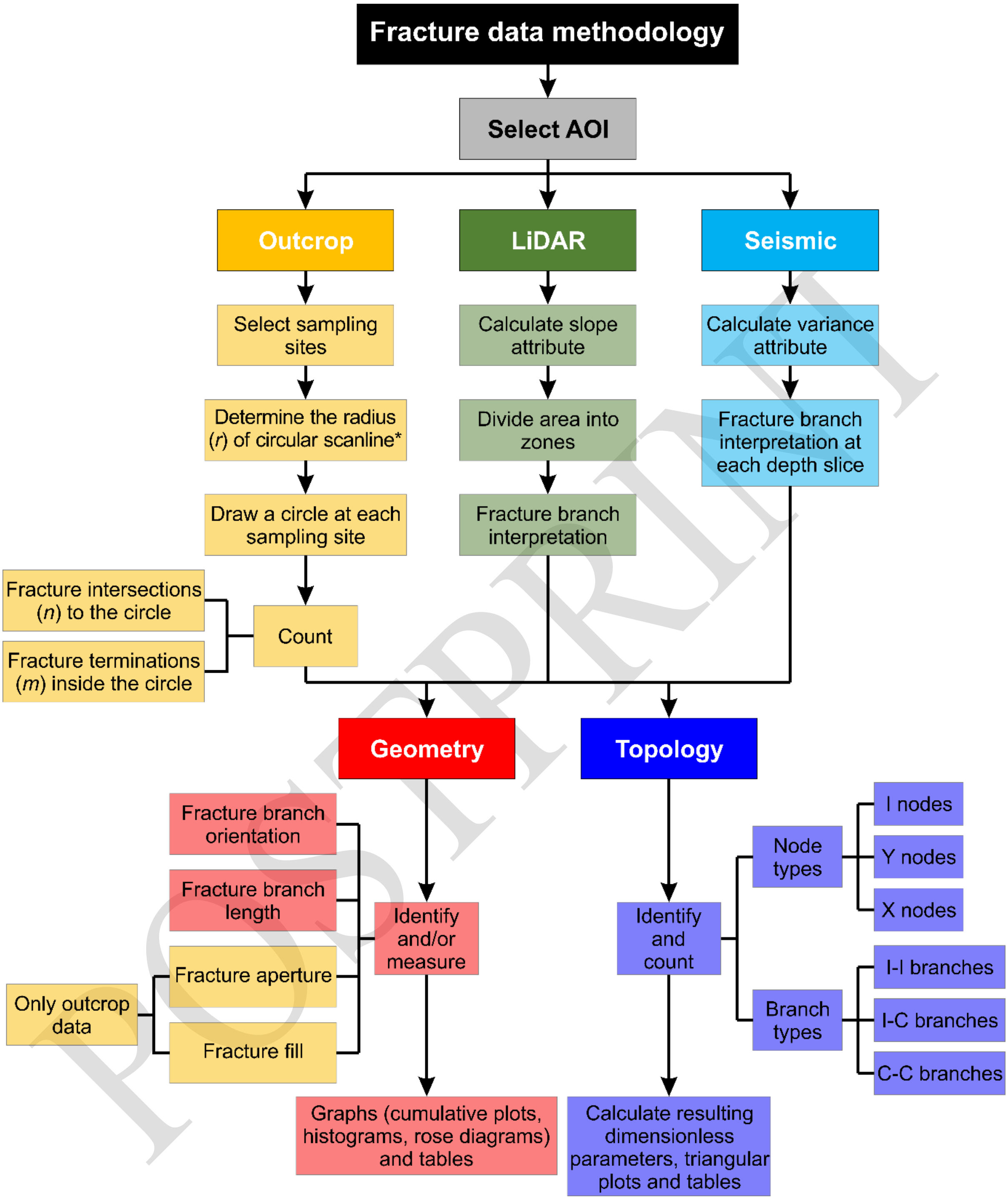
Fracture data methodology
Select AOI
Outcrop
LiDAR
Seismic
Select sampling sites
Calculate slope attribute
Calculate variance attribute
Determine the radius (r) of circular scanline*
Divide area into zones
Fracture branch interpretation at each depth slice
Draw a circle at each sampling site
Fracture branch interpretation
Fracture intersections (n) to the circle
Fracture terminations (m) inside the circle
Count
Geometry
Topology
Fracture branch orientation
Fracture branch length
Fracture aperture
Fracture fill
Only outcrop data
Identify and/or measure
Identify and count
Node types
Branch types
I nodes
Y nodes
X nodes
I-I branches
I-C branches
C-C branches
Graphs (cumulative plots, histograms, rose diagrams) and tables
Calculate resulting dimensionless parameters, triangular plots and tables

Figure 4

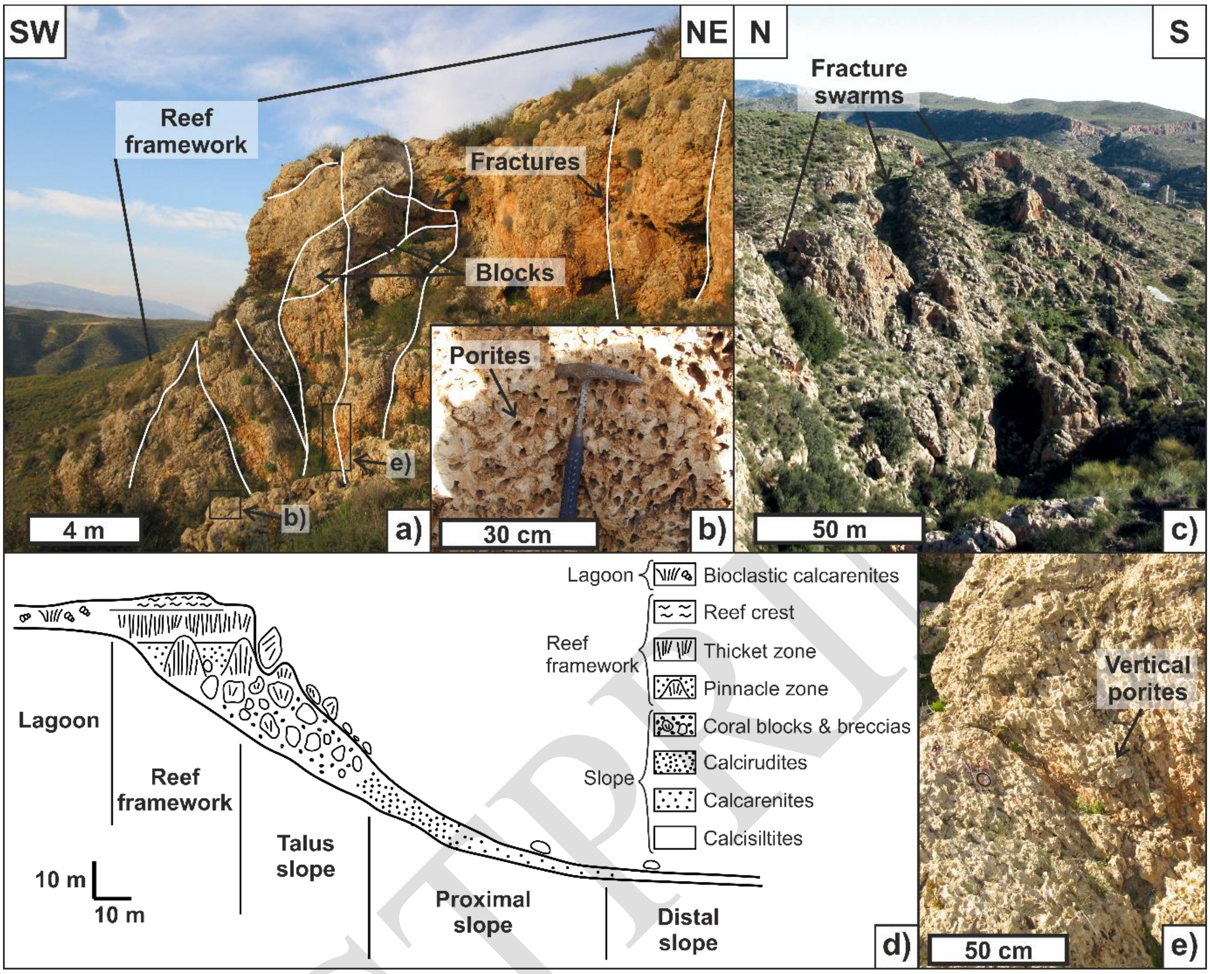
SW
NE
Reef framework
Fractures
Blocks
e)
b)
4 m
a)
Porites
30 cm
b)
N
S
Fracture swarms
50 m
c)
Lagoon
Bioclastic calcarenites
Reef crest
Reef framework
Thicket zone
Pinnacle zone
Coral blocks & breccias
Calcirudites
Slope
Calcarenites
Calcisiltites
Lagoon
Reef framework
Talus slope
Proximal slope
Distal slope
10 m
10 m
d)
Vertical porites
50 cm
e)

Figure 5

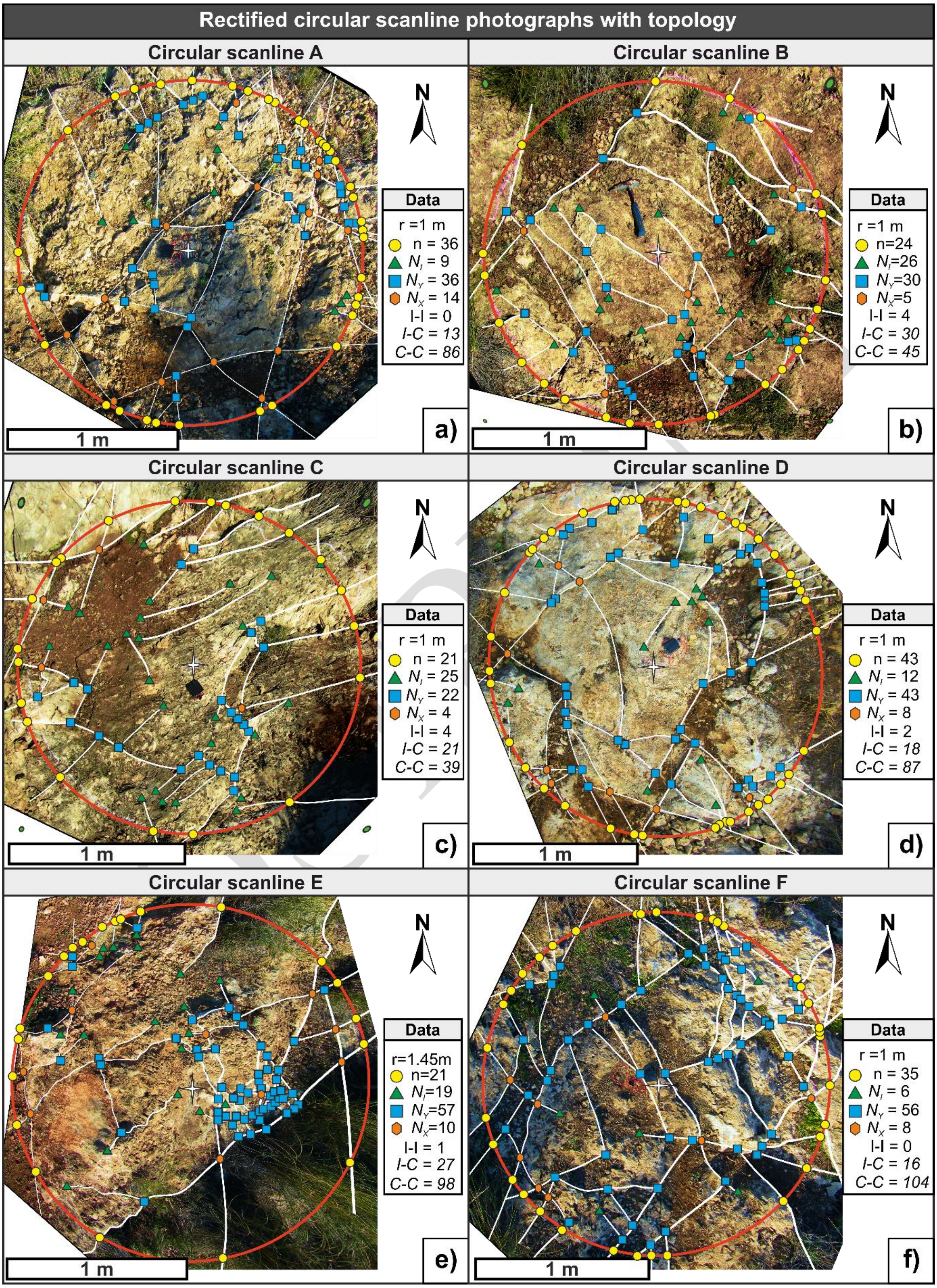
Rectified circular scanline photographs with topology
Circular scanline A
N
Data
r =1 m
n = 36
N_I = 9
N_Y = 36
N_X = 14
I-I = 0
I-C = 13
C-C = 86
1 m
a)
Circular scanline B
N
Data
r =1 m
n=24
N_I=26
N_Y=30
N_X=5
I-I = 4
I-C = 30
C-C = 45
1 m
b)
Circular scanline C
N
Data
r =1 m
n = 21
N_I = 25
N_Y = 22
N_X = 4
I-I = 4
I-C = 21
C-C = 39
1 m
c)
Circular scanline D
N
Data
r =1 m
n = 43
N_I = 12
N_Y = 43
N_X = 8
I-I = 2
I-C = 18
C-C = 87
1 m
d)
Circular scanline E
N
Data
r=1.45m
n=21
N_I=19
N_Y=57
N_X=10
I-I = 1
I-C = 27
C-C = 98
1 m
e)
Circular scanline F
N
Data
r =1 m
n = 35
N_I = 6
N_Y = 56
N_X = 8
I-I = 0
I-C = 16
C-C = 104
1 m
f)

1308 Figure 5. Continued

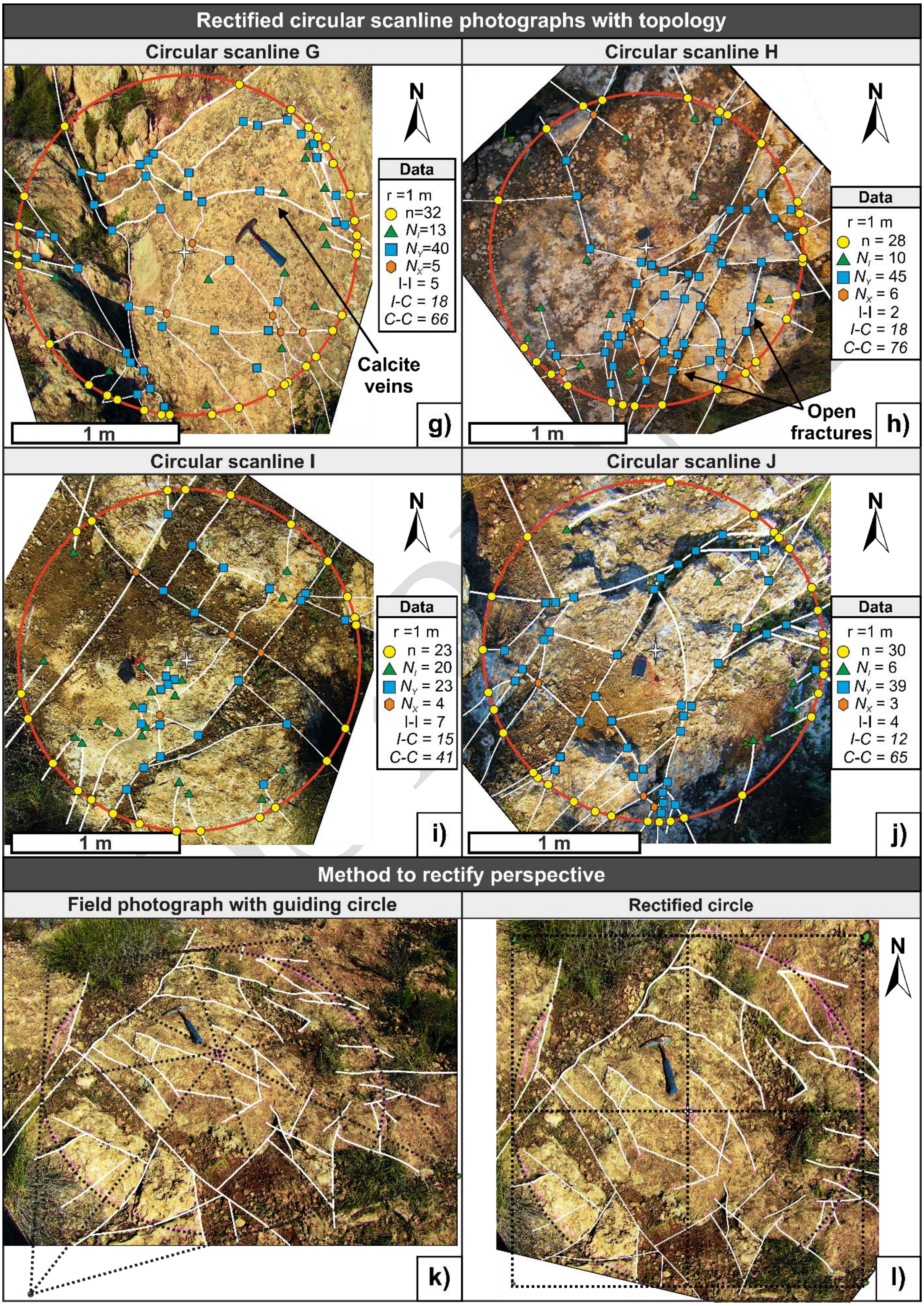

1309

Figure 6

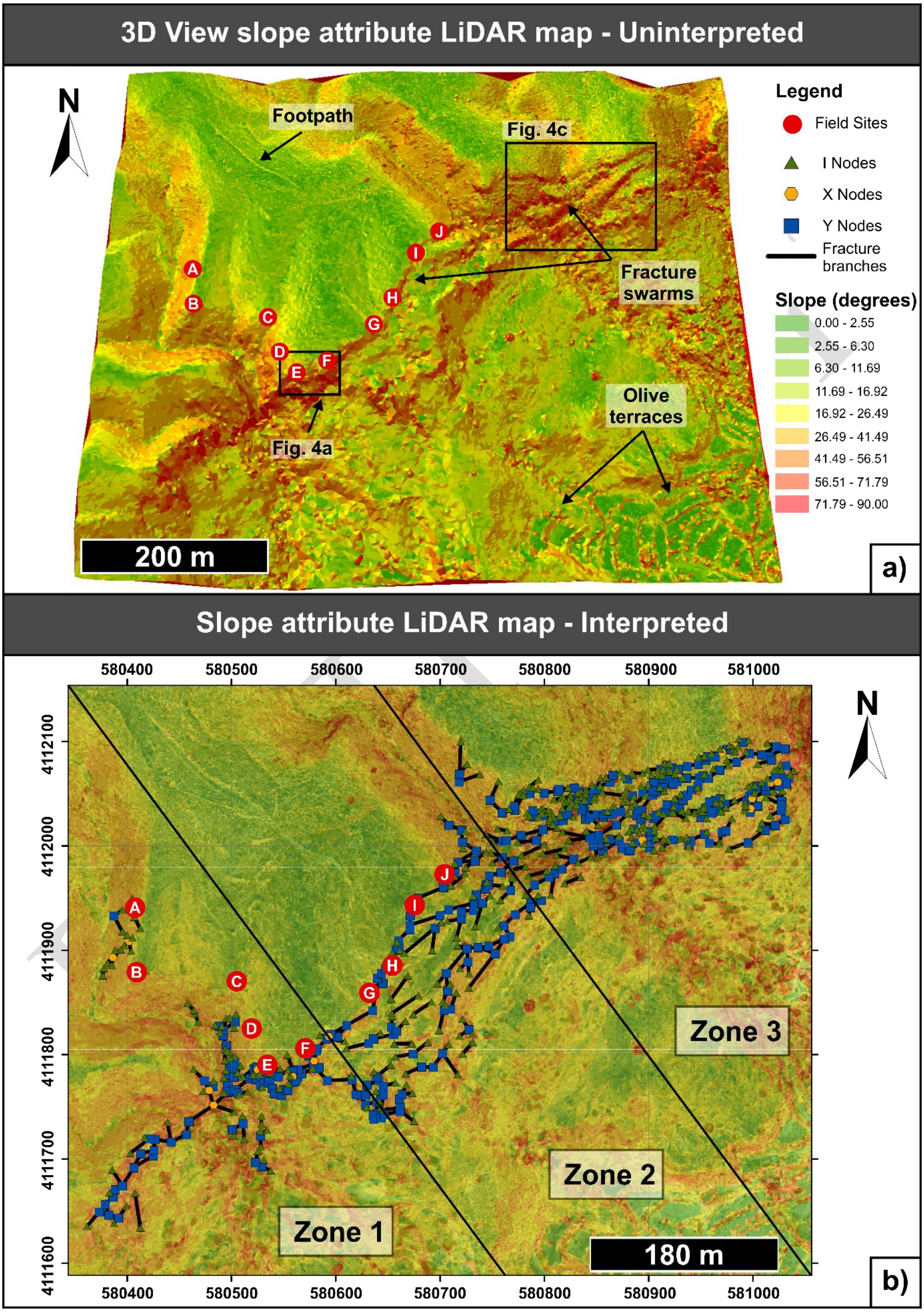
3D View slope attribute LiDAR map - Uninterpreted
N
Footpath
Fig. 4c
Fracture swarms
Olive terraces
Fig. 4a
A
B
C
D
E
F
G
H
I
J
200 m
Legend
Field Sites
I Nodes
X Nodes
Y Nodes
Fracture branches
Slope (degrees)
0.00 - 2.55
2.55 - 6.30
6.30 - 11.69
11.69 - 16.92
16.92 - 26.49
26.49 - 41.49
41.49 - 56.51
56.51 - 71.79
71.79 - 90.00
a)
Slope attribute LiDAR map - Interpreted
580400
580500
580600
580700
580800
580900
581000
4112100
4112000
4111900
4111800
4111700
4111600
N
Zone 1
Zone 2
Zone 3
180 m
b)

1312 Figure 7

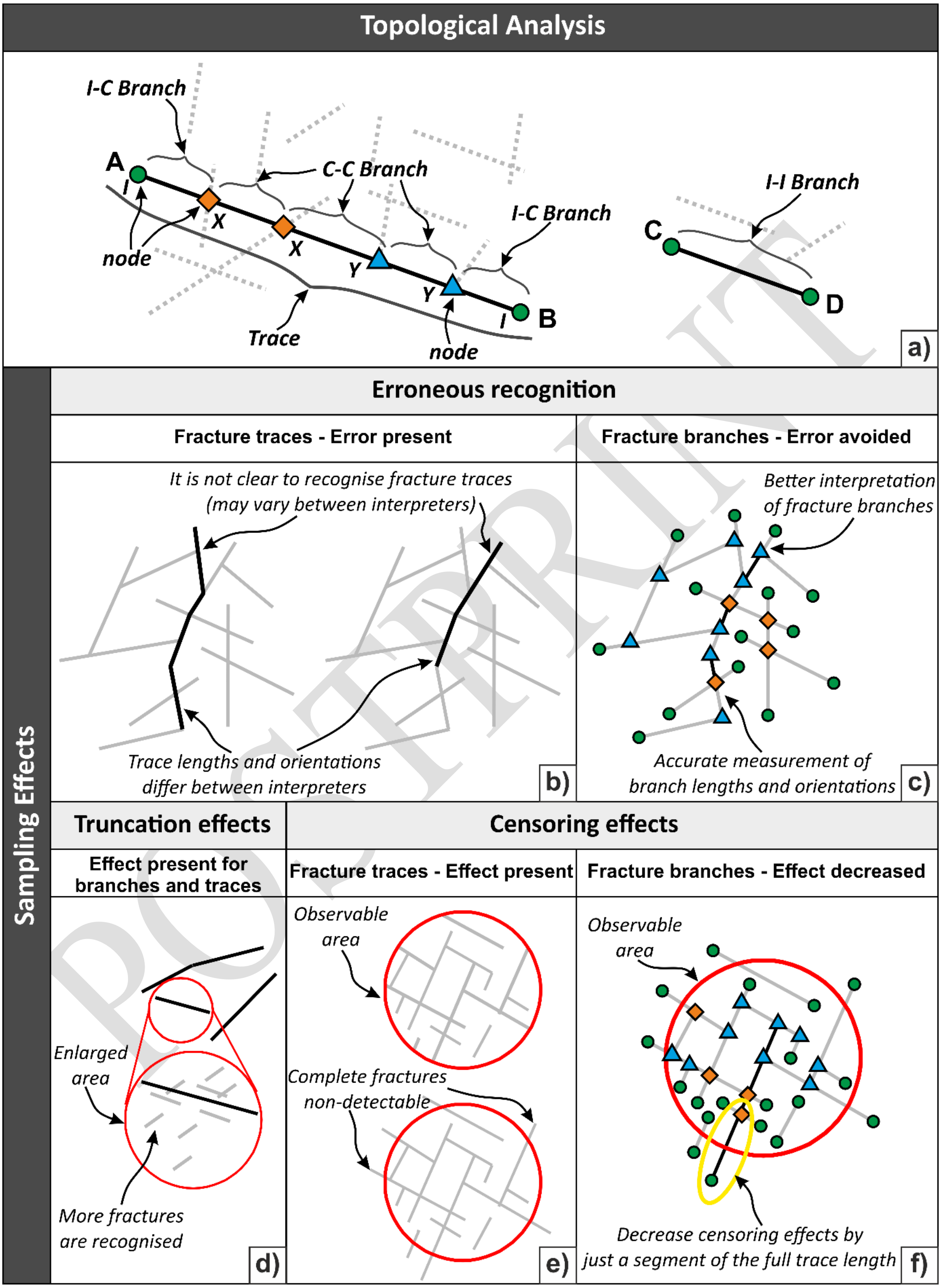

1313

1314

Figure 8

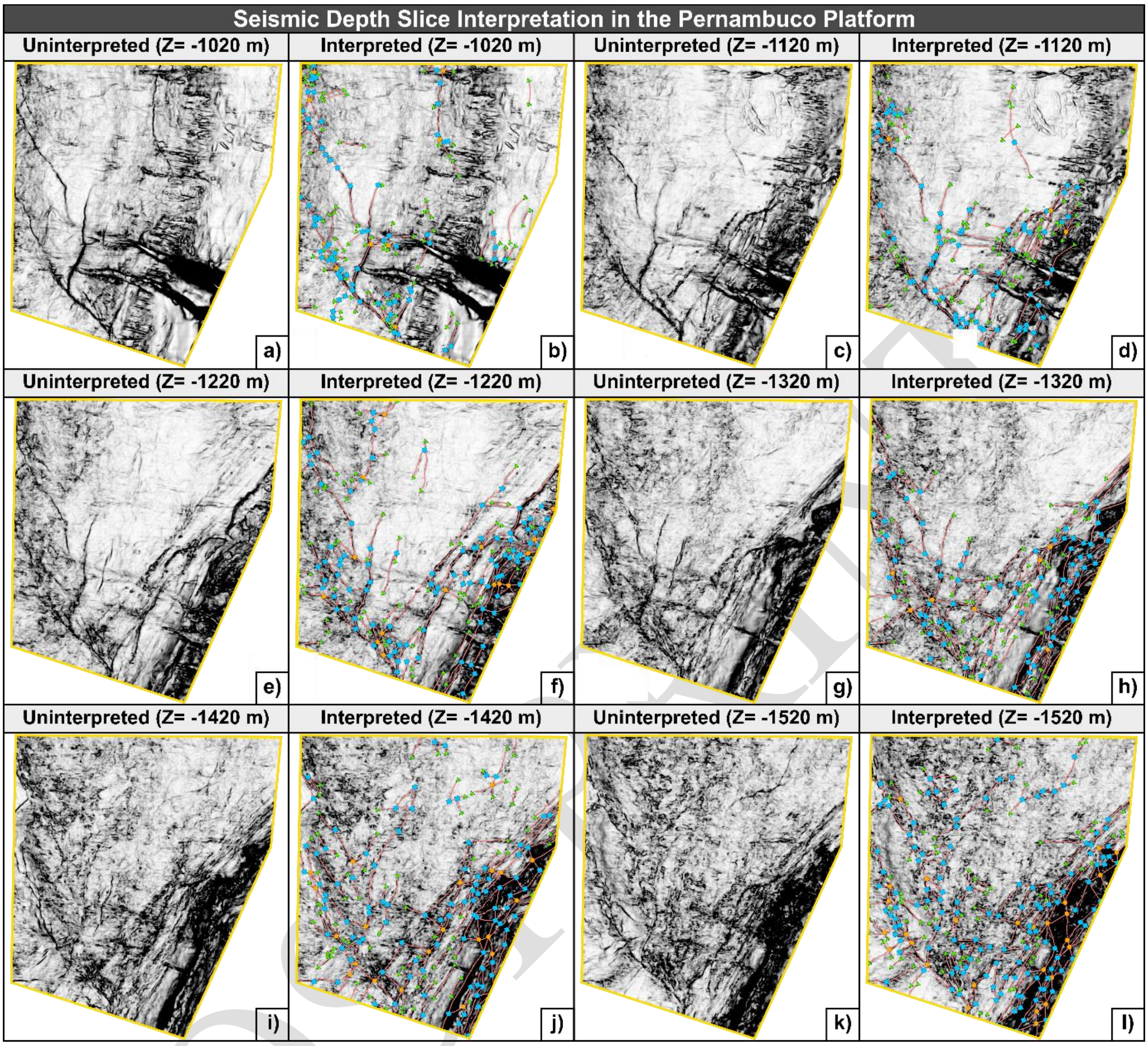
Seismic Depth Slice Interpretation in the Pernambuco Platform
Uninterpreted (Z= -1020 m)
Interpreted (Z= -1020 m)
Uninterpreted (Z= -1120 m)
Interpreted (Z= -1120 m)
a)
b)
c)
d)
Uninterpreted (Z= -1220 m)
Interpreted (Z= -1220 m)
Uninterpreted (Z= -1320 m)
Interpreted (Z= -1320 m)
e)
f)
g)
h)
Uninterpreted (Z= -1420 m)
Interpreted (Z= -1420 m)
Uninterpreted (Z= -1520 m)
Interpreted (Z= -1520 m)
i)
j)
k)
l)

Figure 8. Continued

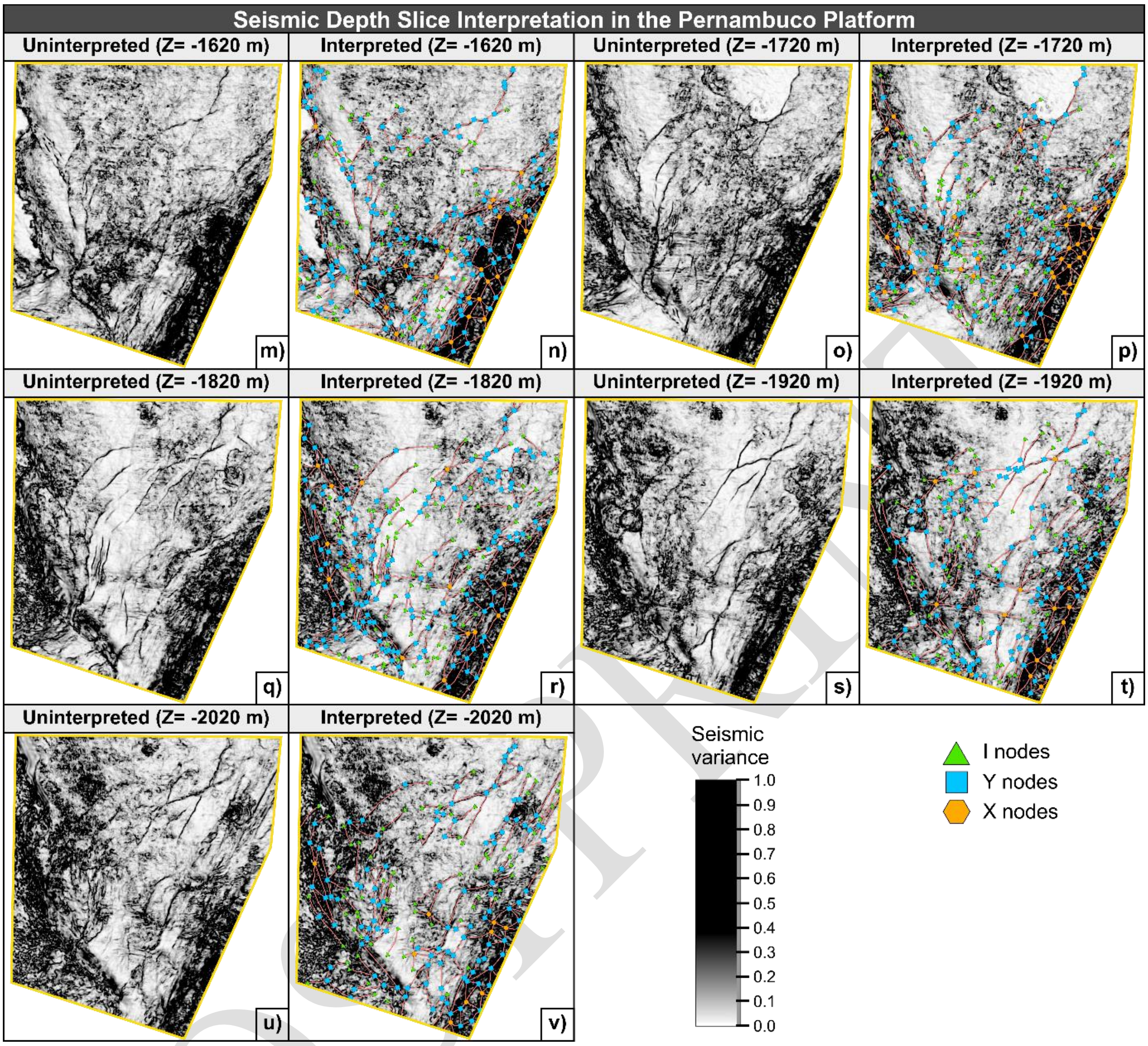

Figure 9

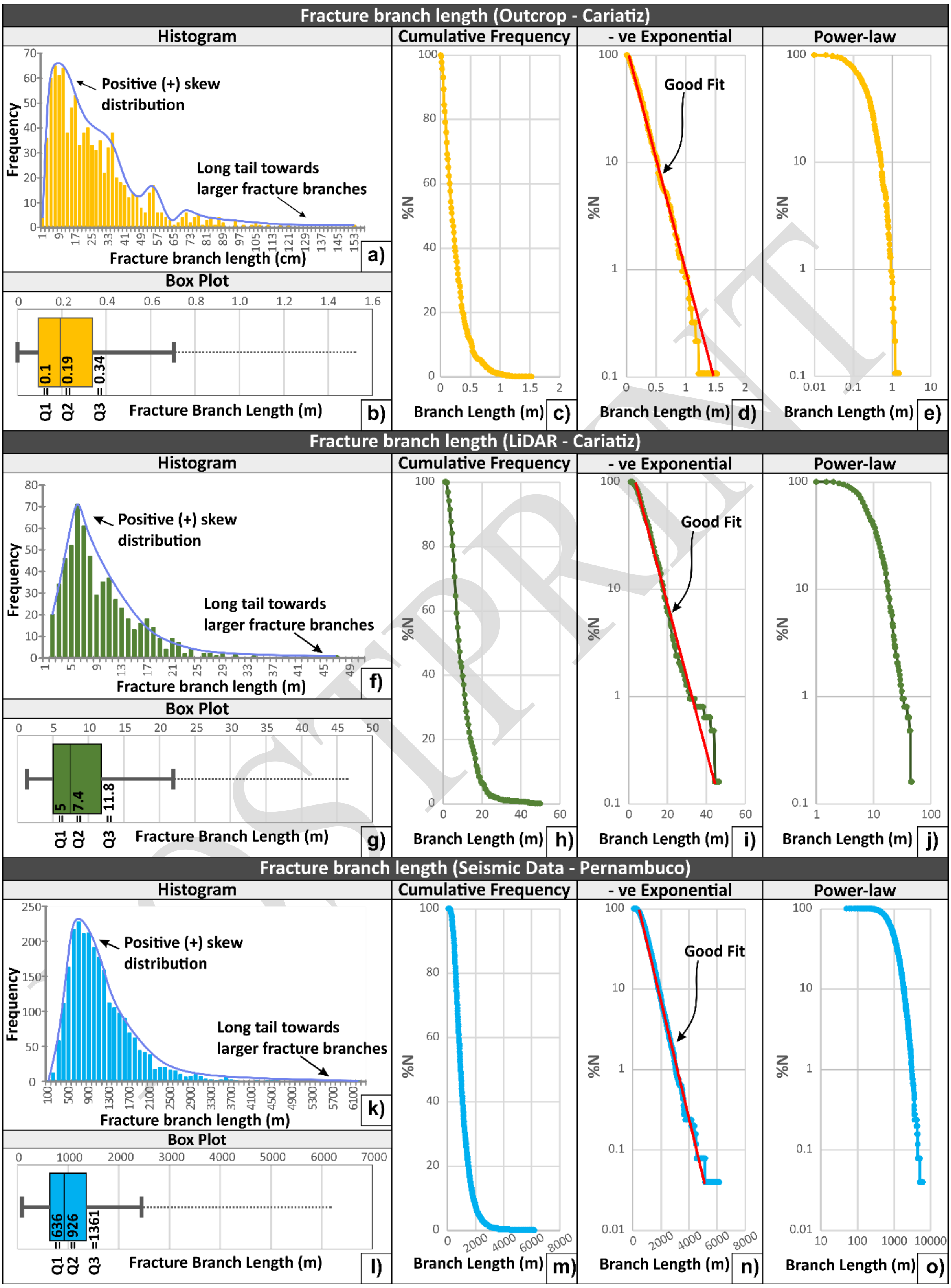

Fracture branch length (Outcrop - Cariatiz)
Histogram
Cumulative Frequency
- ve Exponential
Power-law
Positive (+) skew distribution
Long tail towards larger fracture branches
Frequency
Fracture branch length (cm)
a)
Box Plot
0.1
0.19
0.34
Q1
Q2
Q3
Fracture Branch Length (m)
b)
%N
Branch Length (m)
c)
Good Fit
d)
e)
Fracture branch length (LiDAR - Cariatiz)
Fracture branch length (m)
f)
5
7.4
11.8
g)
h)
i)
j)
Fracture branch length (Seismic Data - Pernambuco)
k)
636
926
1361
l)
m)
n)
o)

Figure 10

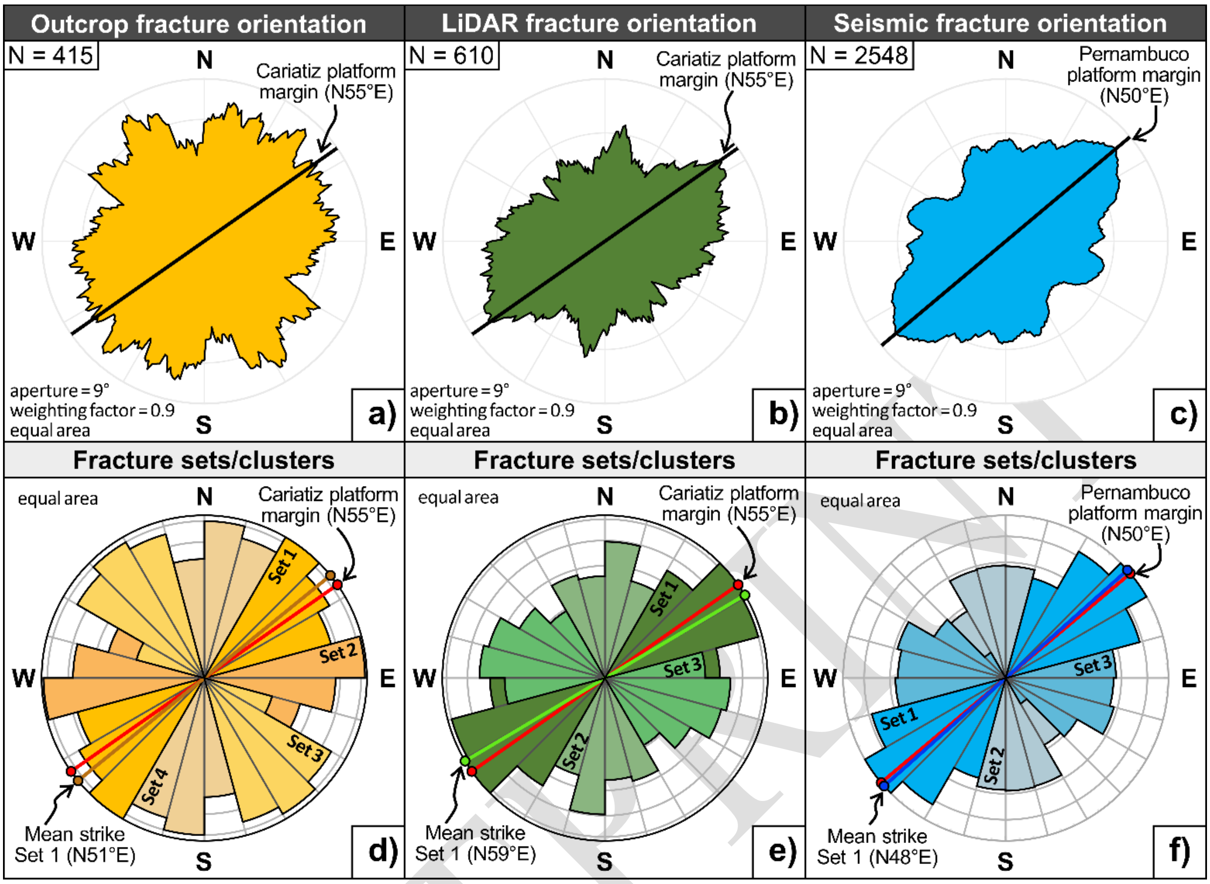

Outcrop fracture orientation
LiDAR fracture orientation
Seismic fracture orientation
N = 415
N = 610
N = 2548
Cariatiz platform margin (N55°E)
Pernambuco platform margin (N50°E)
N
S
E
W
aperture = 9°
weighting factor = 0.9
equal area
a)
b)
c)
Fracture sets/clusters
Set 1
Set 2
Set 3
Set 4
Mean strike Set 1 (N51°E)
Mean strike Set 1 (N59°E)
Mean strike Set 1 (N48°E)
d)
e)
f)

1347 Figure 11

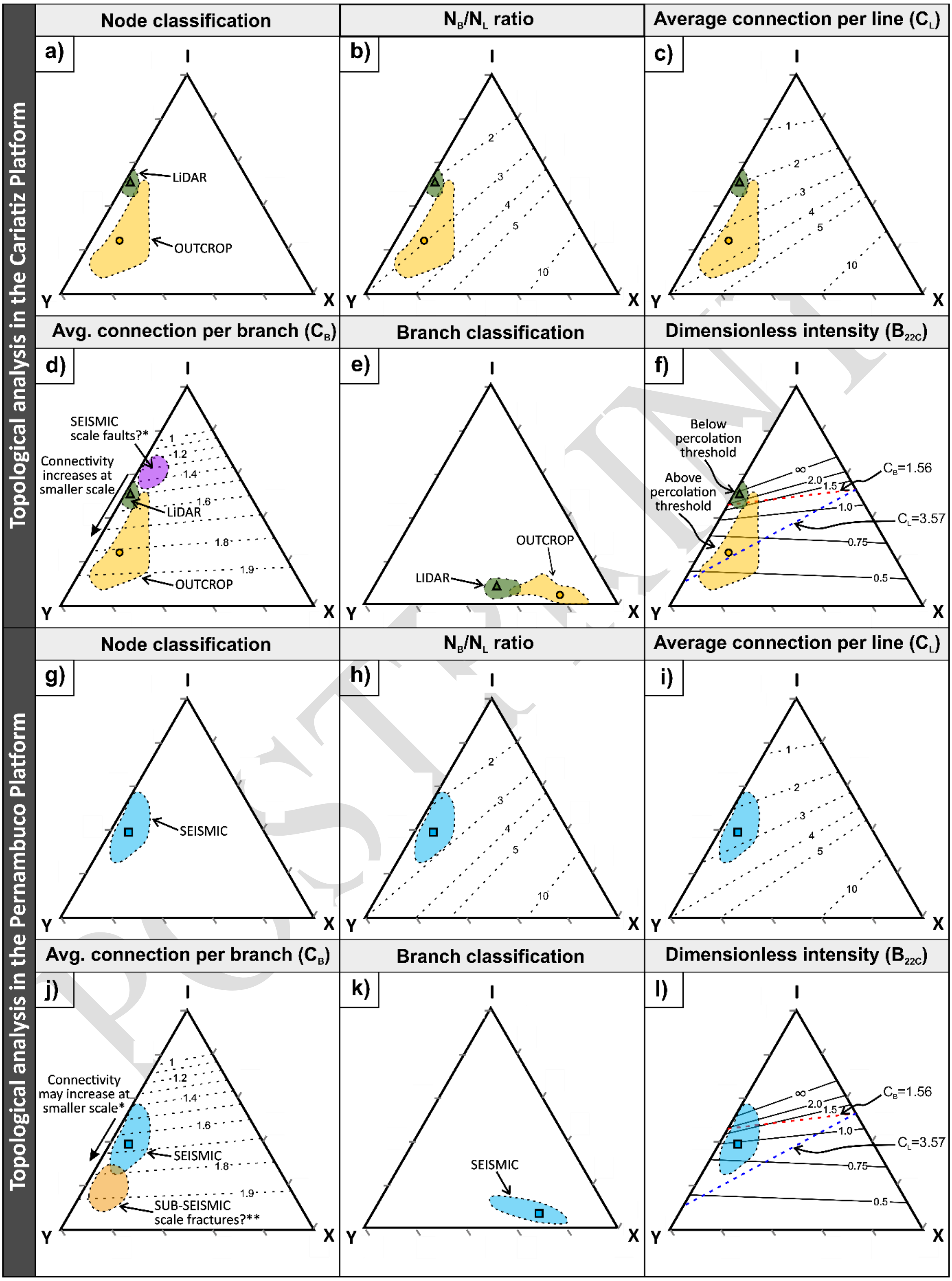

1348

1349

1350 Figure 12

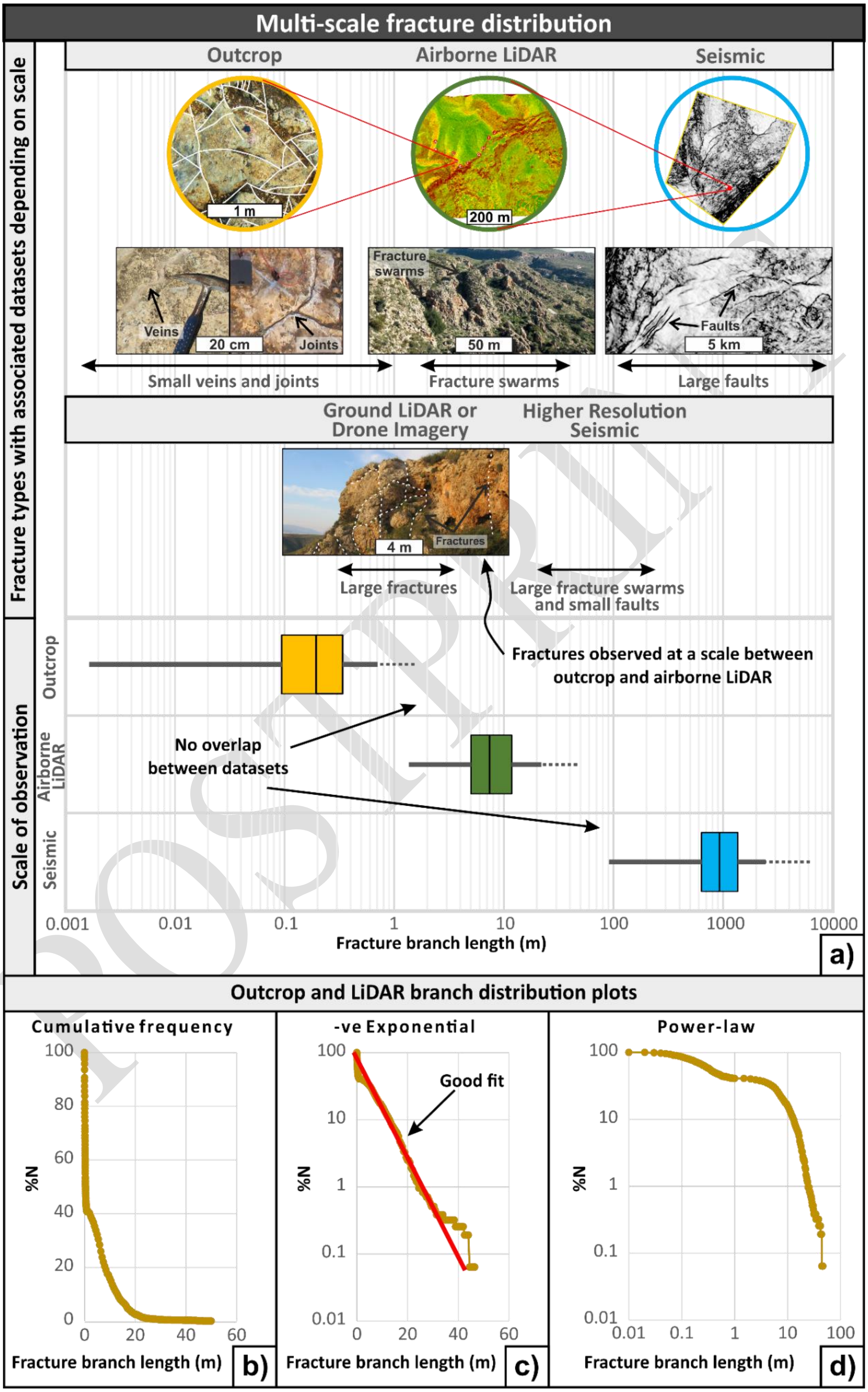

1351

12 Supplementary data

Appendix A. Fracture branch length distribution histograms

Figure A1

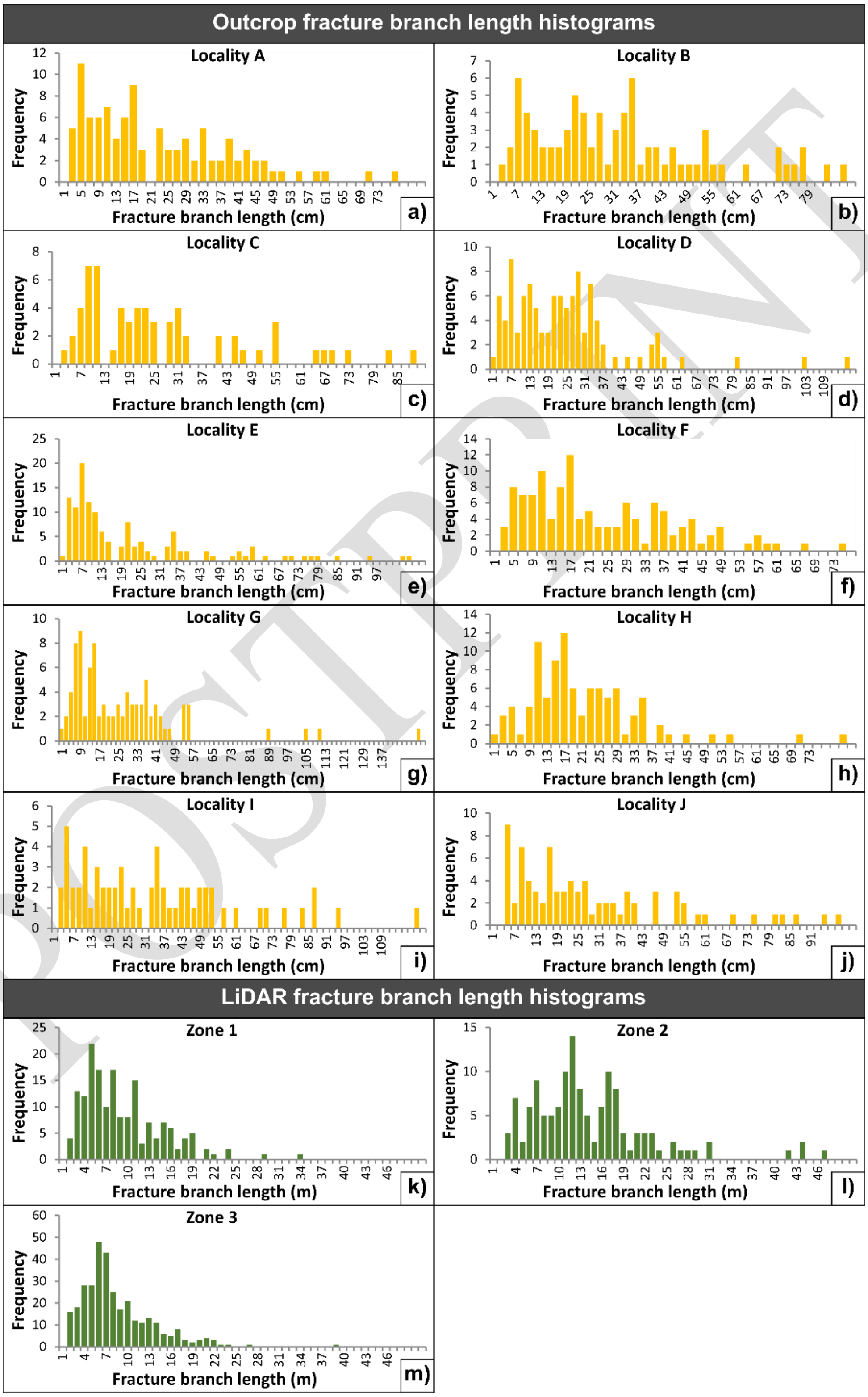

Figure A2

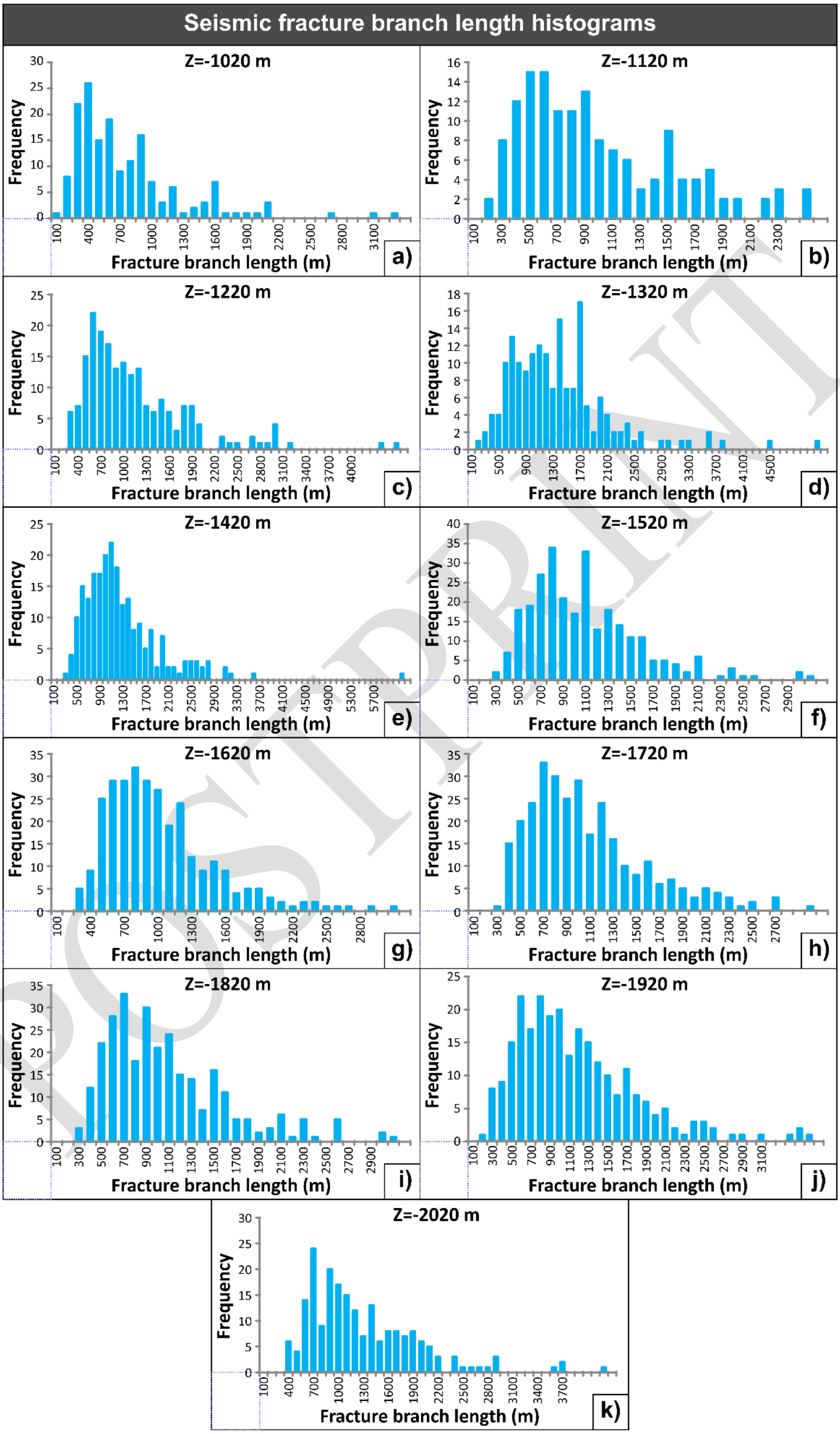
Seismic fracture branch length histograms
Z=-1020 m
a)
Z=-1120 m
b)
Z=-1220 m
c)
Z=-1320 m
d)
Z=-1420 m
e)
Z=-1520 m
f)
Z=-1620 m
g)
Z=-1720 m
h)
Z=-1820 m
i)
Z=-1920 m
j)
Z=-2020 m
k)
Frequency
Fracture branch length (m)

1358 Appendix B. Rose diagrams showing fracture branch orientation

1359 Figure B1

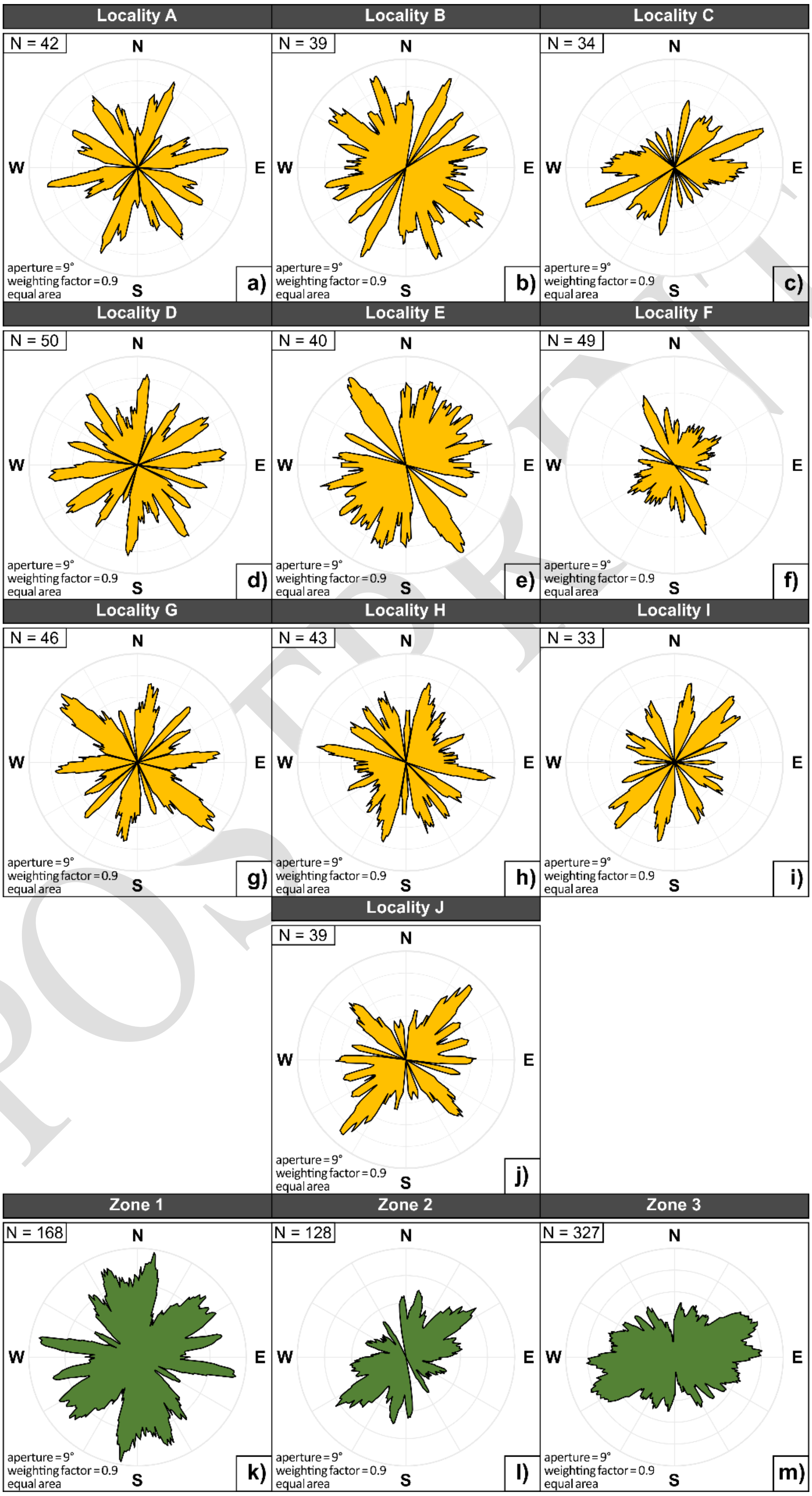

1360

Figure B2

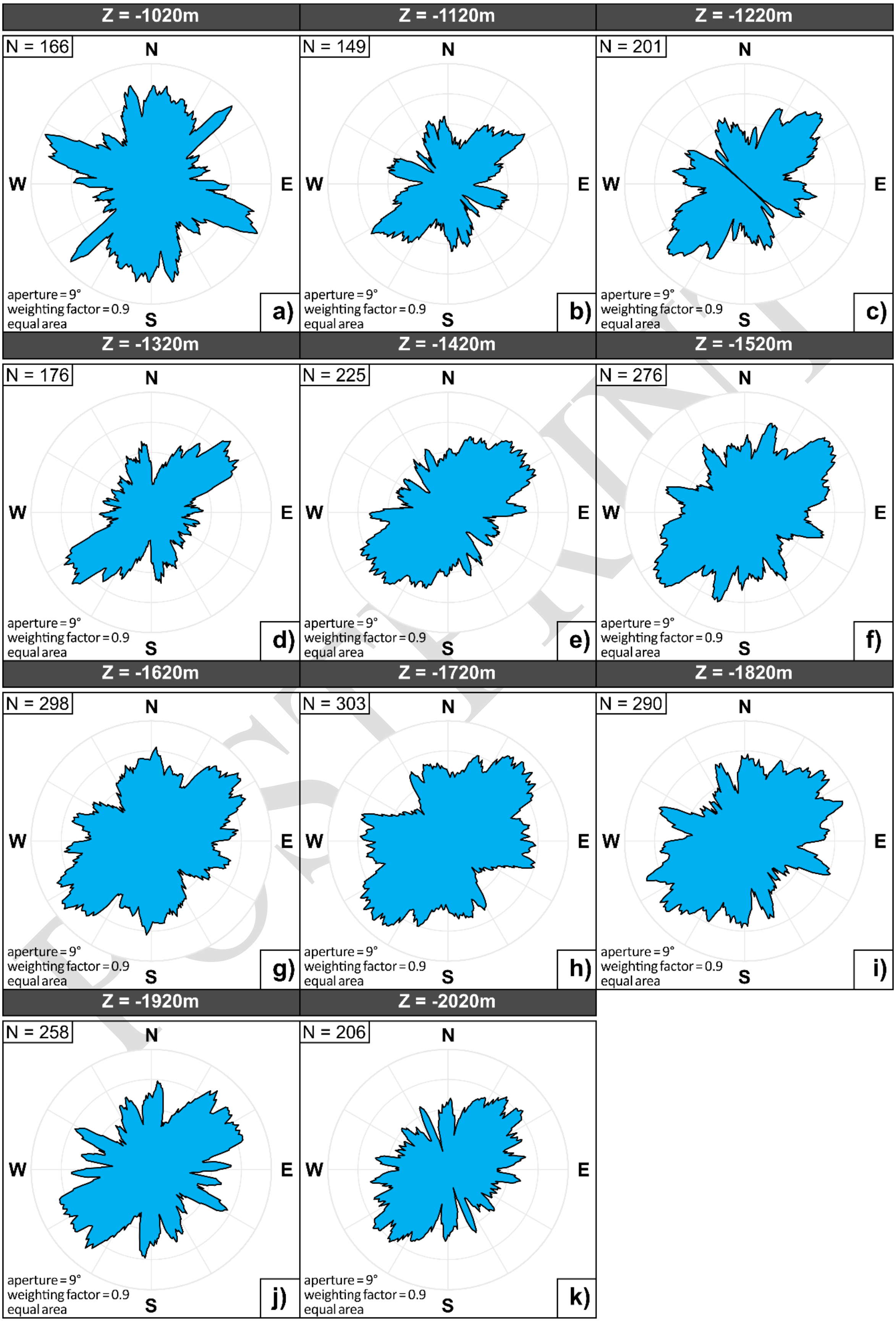
Z = -1020m
N = 166
a)
Z = -1120m
N = 149
b)
Z = -1220m
N = 201
c)
Z = -1320m
N = 176
d)
Z = -1420m
N = 225
e)
Z = -1520m
N = 276
f)
Z = -1620m
N = 298
g)
Z = -1720m
N = 303
h)
Z = -1820m
N = 290
i)
Z = -1920m
N = 258
j)
Z = -2020m
N = 206
k)
N
S
E
W
aperture = 9°
weighting factor = 0.9
equal area

Appendix C. Ternary plots showing detailed topological analyses of nodes and branches

Figure C1

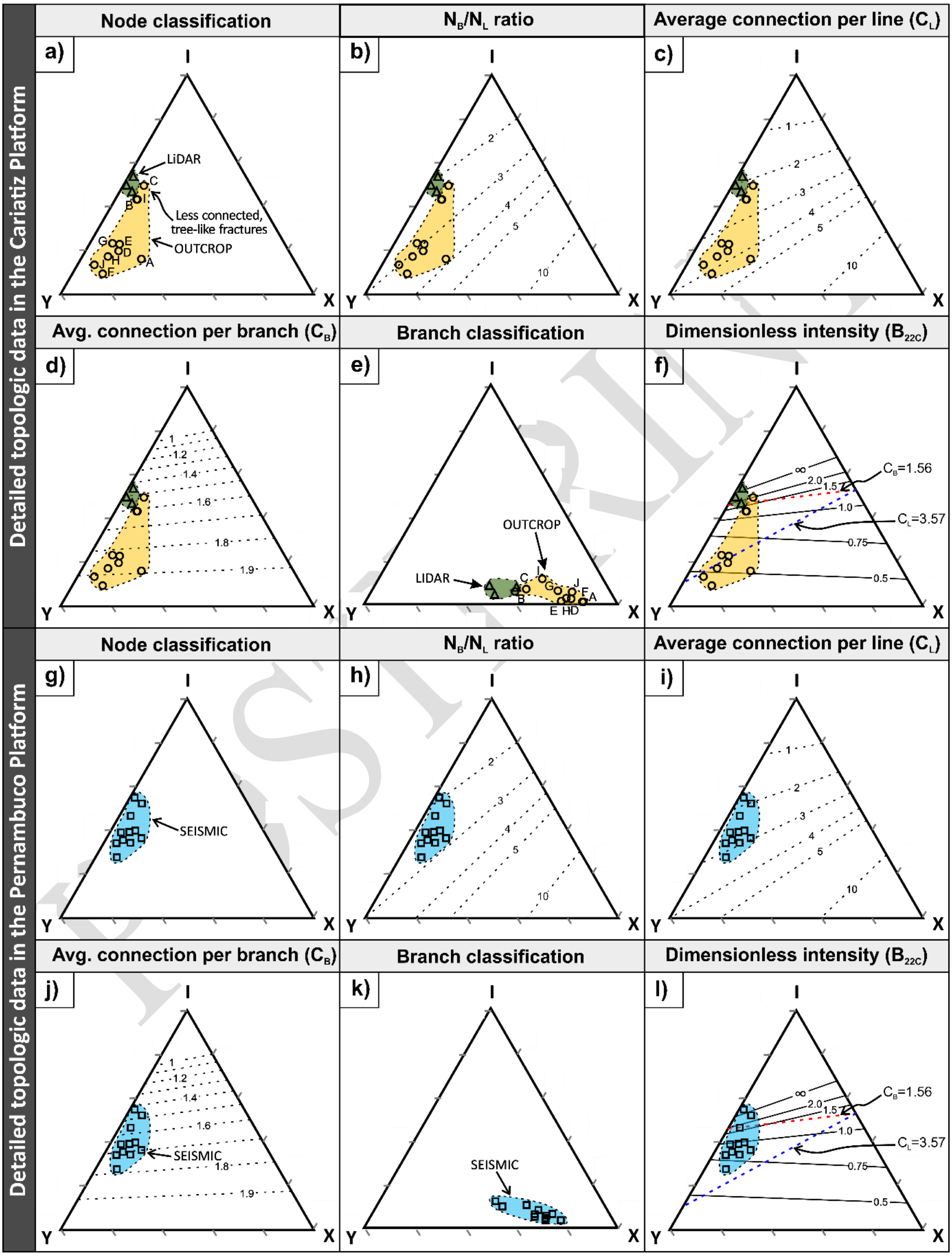

Appendix D. Fracture topological data

Table D1

Parameter	**Notation**	**Equations**
Nodes	*I, Y. X*	Isolated, abutting or splaying, crossing
Number of nodes	N_I, N_Y, N_X	
Branches	*I-I, I-C, C-C*	Isolated, singly-, doubly-connected
Total nodes	N_N	$N_N = N_I + N_Y + N_X$
Total lines	N_L	$N_L = (N_I + N_Y) / 2$
Total branches	N_B	$N_B = (N_I + 3N_Y + 4N_X) / 2$
Branches/Lines	N_B / N_L	$N_B / N_L = (N_I + 3N_Y + 4N_X) / (N_I + N_Y)$
Average connections/line	C_L	$C_L = 2 (N_Y + N_X) / N_L)$
Average connections/branch	C_B	$C_B = (3N_Y + 4N_X) / N_B)$
Branch dimensionless intensity at percolation	B_{22C}	
Probability of isolated nodes	P_I	$P_I = N_I / (N_I + 3N_Y\ 4N_X)$
Prob. connected nodes	P_C	$P_C = (3N_Y + 4N_X) / (N_I + 3N_Y + 4N_X)$
Prob. of isolated branches	P_{II}	$P_{II} = P_I^2$
Prob. of singly connected branches	P_{IC}	$P_{IC} = P_I\ P_C$
Prob. of doubly connected branches	P_{CC}	$P_{CC} = P_C^2$

Table D2

	Node count			Branch count			Number of lines or traces (NL)	Number of branches (NB)	Number of branches to traces ratio (NB/NL)	Total fracture length (FLT)	Average trace length (LL)	Average branch length (BL)	Connections per line or trace (CL)	Connections per branch (CB)	Proportion of nodes		Proportion of branches		
	NI	NY	NX	I-I	I-C	C-C									Isolated (PI)	Connected (PC)	Isolated (PII)	Singly connected (PIC)	Doubly connected (PCC)
Field data (Outcrop)										[cm]	[cm]	[cm]							
Site A	9	36	14	0	13	86	22.5	86.5	3.84	2232.17	99.21	25.81	4.44	1.90	0.0520	0.9480	0.0027	0.0493	0.8987
Site B	26	30	5	4	30	45	28	68	2.43	2436.43	87.02	35.83	2.50	1.62	0.1912	0.8088	0.0365	0.1546	0.6542
Site C	25	22	4	4	21	39	23.5	53.5	2.28	1661.31	70.69	31.05	2.21	1.53	0.2336	0.7664	0.0546	0.1791	0.5873
Site D	12	43	8	2	18	87	27.5	86.5	3.15	2519.18	91.61	29.12	3.71	1.86	0.0694	0.9306	0.0048	0.0646	0.8661
Site E	19	57	10	1	27	98	38	115	3.03	2761.9	72.68	24.02	3.53	1.83	0.0826	0.9174	0.0068	0.0758	0.8416
Site F	6	56	8	0	16	104	31	103	3.32	2749.91	88.71	26.70	4.13	1.94	0.0291	0.9709	0.0008	0.0283	0.9426
Site G	13	40	5	5	18	66	26.5	76.5	2.89	2357.84	88.98	30.82	3.40	1.83	0.0850	0.9150	0.0072	0.0777	0.8373
Site H	10	45	6	2	18	76	27.5	84.5	3.07	1999.34	72.70	23.66	3.71	1.88	0.0592	0.9408	0.0035	0.0557	0.8852
Site I	20	23	4	7	15	41	21.5	52.5	2.44	2096.67	97.52	39.94	2.51	1.62	0.1905	0.8095	0.0363	0.1542	0.6553
Site J	6	39	3	4	12	65	22.5	67.5	3.00	2250.83	100.04	33.35	3.73	1.91	0.0444	0.9556	0.0020	0.0425	0.9131
All outcrop	146	391	67	29	188	707	268.5	793.5	2.96	23065.58	85.91	29.07	3.41	1.82	0.0920	0.9080	0.0085	0.0835	0.8245
Field data (Lidar)										[m]	[m]	[m]							
Zone 1	83	87	8	12	60	92	85	188	2.21	1507.81	17.74	8.02	2.24	1.56	0.2207	0.7793	0.0487	0.1720	0.6072
Zone 2	74	74	0	6	63	66	74	148	2.00	1791.94	24.22	12.11	2.00	1.50	0.2500	0.7500	0.0625	0.1875	0.5625
Zone 3	207	175	6	28	153	147	191	378	1.98	2633.2	13.79	6.97	1.90	1.45	0.2738	0.7262	0.0750	0.1988	0.5274
Lidar	364	336	14	46	276	305	350	714	2.04	5932.95	16.95	8.31	2.00	1.49	0.2549	0.7451	0.0650	0.1899	0.5552
Seismic data										[m]	[m]	[m]							
-1020 m	97	78	11	15	67	83	87.5	187.5	2.14	119340.04	1363.89	636.48	2.03	1.48	0.2587	0.7413	0.0669	0.1918	0.5496
-1120 m	96	76	3	17	62	68	86	168	1.95	139308.08	1619.86	829.21	1.84	1.43	0.2857	0.7143	0.0816	0.2041	0.5102
-1220 m	78	106	15	9	60	132	92	228	2.48	220090.82	2392.29	965.31	2.63	1.66	0.1711	0.8289	0.0293	0.1418	0.6872
-1320 m	87	92	8	17	53	104	89.5	197.5	2.21	234830.78	2623.81	1189.02	2.23	1.56	0.2203	0.7797	0.0485	0.1717	0.6080
-1420 m	88	112	21	12	65	145	100	254	2.54	275457.57	2754.58	1084.48	2.66	1.65	0.1732	0.8268	0.0300	0.1432	0.6836
-1520 m	89	144	27	8	73	195	116.5	314.5	2.70	286638.22	2460.41	911.41	2.94	1.72	0.1415	0.8585	0.0200	0.1215	0.7370
-1620 m	76	176	23	8	60	228	126	348	2.76	288439.9	2289.21	828.85	3.16	1.78	0.1092	0.8908	0.0119	0.0973	0.7935
-1720 m	101	139	38	12	78	212	120	335	2.79	308308.35	2569.24	920.32	2.95	1.70	0.1507	0.8493	0.0227	0.1280	0.7212
-1820 m	95	170	14	16	64	208	132.5	330.5	2.49	296778.68	2239.84	897.97	2.78	1.71	0.1437	0.8563	0.0207	0.1231	0.7332
-1920 m	88	143	17	12	64	180	115.5	292.5	2.53	287458.13	2488.81	982.76	2.77	1.70	0.1504	0.8496	0.0226	0.1278	0.7218
-2020 m	84	122	9	15	54	132	103	243	2.36	254034.02	2466.35	1045.41	2.54	1.65	0.1728	0.8272	0.0299	0.1430	0.6842
All seismic	979	1358	186	141	700	1687	1168.5	2898.5	2.48	2710684.59	2319.80	935.20	2.64	1.66	0.1689	0.8311	0.0285	0.1404	0.6908